5-13-2022

Analysis and implementation of low fidelity radar-based remote sensing for unmanned aircraft systems

Matthew Duck
Mississippi State University, mwd116@msstate.edu

Analysis and implementation of low fidelity radar-based remote sensing for unmanned aircraft systems

By

Matthew Duck

Approved by:

Ali Gurbuz (Major Professor)
Mehmet Kurum
J. Patrick Donohoe
Qian (Jenny) Du (Graduate Coordinator)
Jason M. Keith (Dean, Bagley College of Engineering)

A Thesis
Submitted to the Faculty of
Mississippi State University
in Partial Fulfillment of the Requirements
for the Degree of Master of Science
in Electrical and Computer Engineering
in the Department of Electrical and Computer Engineering

Mississippi State, Mississippi

May 2022

Name: Matthew Duck

Date of Degree: May 13, 2022

Institution: Mississippi State University

Major Field: Electrical and Computer Engineering

Major Professor: Ali Gurbuz

Title of Study: Analysis and implementation of low fidelity radar-based remote sensing for unmanned aircraft systems

Pages of Study: 110

Candidate for Degree of Master of Science

Radar-based remote sensing is consistently growing, and new technologies and subsequent techniques for characterization are changing the feasibility of understanding the environment. The emergence of easily accessible unmanned aircraft system (UAS) has broadened the scope of possibilities for efficiently surveying the world. The continued development of low-cost sensing systems has greatly increased the accessibility to characterize physical phenomena. In this thesis, we explore the viability and implementation of using UAS as a means of radar-based remote sensing for ground penetrating radar (GPR) and polarimetric scatterometry. Additionally, in this thesis, we investigate the capabilities and implementations of low-cost microwave technologies for applications in radar-based remote sensing compared to higher fidelity and more expensive technologies of similar scope.

Key words: Ground Penetrating Radar , Unmanned Aircraft System, Scatterometer, Microwave Remote Sensing

ACKNOWLEDGEMENTS

I would like to thank both Dr. Ali Gurbuz and Dr. Mehmet Kurum for their guidance and expertise in developing my radar and processing systems. Their insight into the needs, physics, and technical requirements of these systems was immeasurable, and it was greatly appreciated. I have learned a tremendous amount under their leadership as a member of the Information Processing and Sensing (IMPRESS) Laboratory, and I am very grateful for my time.

I would like to thank my colleagues in the IMPRESS Lab, specifically Austin, Ben, and Mehedi for their assistance in the development of my radar systems, and for helping with the data collection of my ground based and UAS based systems. The project requirements were extensive and their design input and assistance in the creation of my systems was invaluable. I would like to thank JR Jamora for his assistance and partnership over the last four years in the help of this research project.

Lastly, I would like to thank my family. To my parents and brother, thank you for always supporting my ambitions and pushing me to achieve my goals. To Manny, thank you for instilling in me a desire to become an engineer and fostering my passion for math and science at an early age.

TABLE OF CONTENTS

LIST OF TABLES

LIST OF FIGURES

LIST OF SYMBOLS, ABBREVIATIONS, AND NOMENCLATURE

MRS Microwave Remote Sensing

UAS Unmanned Aircraft System

EM Electromagnetic

FOV Field of View

SFCW Stepped-Frequency Continuous Wave

GPS Global Positioning System

GPR Ground Penetrating Radar

LIDAR Light Detection and Ranging

RF Radio Frequency

USB Universal Serial Bus

CPU Central Processing Unit

SA Spectrum Analyzer

SCPI Scientific Computer Programming Interface

VNA Vector Network Analyzer

TOI Target of Interest

UAV Unmanned Aerial Vehicle

UAS Unmanned Aircraft System

CHAPTER I

INTRODUCTION

1.1 Motivation

Microwave remote sensing (MRS), specifically radar, has adapted over the last 80 years to be a widely used tool in many fields of research including archaeological excavation, structural engineering, agricultural sciences, weather tracking, global imaging, and target detection. However, while MRS technology becomes more advanced and grows in technical robustness, its ability to compete with the harsh environment has not grown as rapidly. Many radars, like ground penetrating radar (GPR), have been predominately implemented from the ground with automotive vehicles, light-weight carts, or handheld equipment as the means of usability. This means of housing and operating radar technology, while functional and robust, harbors a moderate level of concern and a suite of obstacles for both speed and safety of data collection. Harsh environments including rugged terrain, steep mountain sides, and marshy fields make radar a difficult tool to implement without endangering both the equipment and the researcher(s) surveying the location. Additionally, traversing a non-ideal environment from the ground presents problems with the speed at which data can be collected. Ground-based radar tools that can quickly survey a large area are often expensive, and are still not capable of being used in a wide variety of environments, usually designed to be functional in highly specific situations.

There have also been many radar systems, such as scatterometers, implemented from high altitudes such as space-born satellites and air crafts. This allows the radar to image large swaths of area from tens of kilometers wide to hundreds of kilometers wide for applications like soil moisture characterization, vegetative health analysis, and surface current tracking over the ocean. While this means of implementation is beneficial for characterizing large areas of interest, it is not ideal for imaging areas less than a few hundred meters in size, such as an agricultural field.

The emergence of unmanned aircraft systems (UAS) has grown in the last few decades to be a low cost and easily accessible tool for uses in radar applications. As UAS-based radar is implemented from the air, it is not limited to the topographical issues that ground-based radar is and can be used over any type of terrain and environment. As they are not bound by the physical characteristics of the ground, UAS can quickly traverse over a large area. This technology offers a new avenue of feasibility for radar research which will be investigated in the document.

1.2 Literature Review

As discussed in Section 1.1, UAS-based radar is advantageous over more traditional ground-based approaches for its ability to traverse over any terrain regardless of topography which can increase travel speed while imaging as well as its capabilities for imaging small-scale areas of interest that traditional aerial-based radars can not image due to resolution issues at extreme altitudes. A UAS-based implementation is seen in Ludeno et. al's approach [22] where the team focused on the design of a microwave radar for micro-UAV for tomographic imaging as a means of characterizing an inaccessible area quickly. This work was done with a low-cost ultra-wide band pulse radar system between 3.1GHz and 4.8GHz which was designed to be viable for use on the

UAV for its small form factor. The data processing was able to mitigate the altitude variations from the UAS instability by capturing and removing the first echo from the radar's time domain response which made the targets more visible in post-processing.

The application of radar for UAS-based approaches has been investigated for use in synthetic aperture radar (SAR) imaging by Lort et.al [21] where the team investigated SAR capabilities for UAV applications to determine its potential for future implementations. The team designed a polarimetric X-band radar equipped to UAV. The radar is capable of 30dBm transmit power and resolves its returns with 1.5m resolution. Testing was performed in agricultural areas with suburban scenes such as houses and cars. The team used various calibration targets including trihedral reflectors and was able to generate sufficient polarimetric responses that lined up with the theoretical responses of the calibration with the UAV payload. Further, Yan et. al designed a UAV-based SAR system [33] with the purpose of validating the design and implementation of a low-cost sensing for UAV-based applications. The team was able to collect real-time data and characterize target features of a construction site. This testing shows both the reliability and viability of UAV-based radar use for sensing systems.

Applications of UAS-based radar include extensive work for soil moisture measurements. Simpson et. al developed a UAS-based radar [27] for soil moisture characterization between 2-6 GHz using an ultra-linear chirp waveform. The team also developed a SAR processing algorithm for imaging the surface by dividing the data into multiple apertures across the azimuth plane. The testing showed a near-perfect impulse response with moderate SNR. Kaundinya et. al also created an ultra-wideband radar system (2-18GHz) [18] designed for soil moisture measurements equipped for an unmanned aerial system (UAS). A radar test bed was developed with a chirp

waveform generator to transmit through a four micro-strip antenna array. The test setup monitored the response between wet and dry soil with varying polarizations at different incidence angles. The consensus of the experiments is the system can discern approximately 5% water content variance in the soil. This shows that soil moisture content was adequately characterized by the UAS-based radar. Wu et. al developed a UAV-based GPR [32] for soil moisture measurements. The GPR was tested in agricultural fields in Belgium to characterize the soil moisture content with testing lasting less than 15 minutes. The soil moisture response showed to be similar to the elevation maps of the fields considering flight instabilities and antenna reflections.

With the advancement of UAS-based radar, there are interests in its applications using GPR. Badjou et. al developed a drone-based GPR design [13] for humanitarian applications such as search and rescue after floods or earthquakes. This design includes a waveform generator and Vivaldi antennas. The testing shows consideration for the drone's flight speed to limit speeds to 1m/s as potentially moving targets, like people, could introduce Doppler aliasing at faster flight speeds. UAS-based GPR also has potential for landmine detection shown by the research of Šipoš et.al [28] where a drone-based GPR for landmine detection is developed. The team investigated methods to overcome the intricacies of a frequency domain waveform like frequency-modulated continuous wave (FMCW), using a time domain pulse radar to obtain the frequency span and to best yield moderate spatial resolution. This is done with a pulse generation circuit and an avalanche transistor along with Vivaldi/horn hybrid antennas used for transmission. The testing setup involved moving the GPR over the ground 1.5m above the surface across a rail and moving at 1m/s with a metal object placed above the surface at 0.6m. This testing shows the GPR being capable of obtaining a moderate response from the target. Further, Fernandez et developed a UAV-

based GPR [15] that utilizes SAR algorithms for landmine detection. The team leveraged the SAR algorithms for the imaging of the subsurface along with clutter removal techniques for mitigating the impedance mismatching of the air and soil. To mitigate altitude instability the team leverages real-time kinematic (RTK) sensors and LIDAR altitude sensors for altimeter ranging. The team buried an 8cm circular metal sheet and a 5cm diameter cylinder 12cm below sand for testing and was able to resolve 2-2.5cm range resolution. The project shows good results in applications of detecting structural defects in walls, roofs, and roads and can be deployed quickly with use on a UAV.

The methods for transmission and processing of GPR have also been explored for use with a UAS. Carey in his thesis [14] develops a stepped-frequency continuous wave (SFCW) GPR using a software defined radio (SDR). This approach uses two daughter boards to create the transmit and receive chains. The FPGAs on board require precise scheduling between the two daughter boards which coupled with two LNAs on the receive chain makes it difficult and requires system calibration to align the data acquisition of the GPR. The GPR is tested with metal spheres placed above and below the surface. The data shows the GPR can adequately characterize the spheres at 28.5cm below the surface. Carey also tests other targets such as brick and surrogate landmines which are also detected in the GPR response. Additionally, Uduwawala [29] investigates the advantages and disadvantages of a Gaussian pulse compared to a differentiated Gaussian pulse for pulse radar based GPR. The testing done shows that a Gaussian pulse has a lower clutter level than the differentiated Gaussian pulse. The differentiated Gaussian pulse has a better signal strength than the Gaussian pulse. Uduwawala concludes that the differentiated Gaussian pulse is more suitable for detecting

targets that are buried deep and uniformly placed in a surface whereas the Gaussian pulse is more suited for shallow depth targets with high spatial resolution.

UAS-based radar also has applications in scatterometry for characterization of soil moisture content. Soil moisture characterization using SAR can be difficult as the surface roughness of the scene causes errors and ground-based scatterometers have shown the ability to mitigate these issues. Kwon et. al investigated the inversion of the scattering parameters [20] obtained from a VNA-based scatterometer and SAR imagery was used to characterize soil moisture and surface roughness of a soybean field. Wu et. al developed a ground-based scatterometer [31] for soil moisture characterization. Two tests were conducted with a FMCW scatterometer with various soil moisture contents from 20% to 37% moisture content. The results showed the 37% moisture content matched best with the theoretical backscatter models. Qiu et. al [24] studied the inversion of a ground based scatterometer backscatter response for soil moisture characterization. The team used the Integral Equation Model (IEM) to map the soil moisture content. The data shows that the IEM and true data line up well with error between 4.6%-13.7% validating the ground based scatterometer is viable with the surface roughness removed.

There has been research done to determine the accuracy of low-altitude scatterometers for soil moisture mapping. Jia et. al [17] investigated the sensing of rice fields in China circa 2009 using a ground-based scatterometer. The intent of the system was to monitor the growth of the rice plant compared to known information regarding the biomass and the leaf area index (LAI). Testing was done in the L, C, X and S frequency bands, at 10, 30, 53, 72, and 95 days of growth and with full polarization at varying incident angles between 0 and 90 degrees. Another set of tests was conducted at a static incident angle of 35 degrees over the growth period of the rice

to measure the backscatter of all polarizations in all frequency bands as compared to the rice biomass response. Finally, a similar test was done to compare the backscatter response to the lead area index of the rice plant. Goswami et. all discusses the analysis of scatterometer backscatter responses. The team's system operates at 9.48GHz and operated at varying incident angles between 25-70 degrees. The data collected was compared to the gravimetric soil moisture readings and the backscatter coefficients were found to best align at an incident angle of 35 degrees [16].

1.3 Novelty and Contributions

This thesis will focus on the development of three radar systems: a UAS-based GPR, a UAS-based scatterometer, and a ground-based scatterometer.

The novelty of the UAS-based GPR is that it is implemented from a drone which mitigates the issues intrinsic in traversing harsh terrain with a ground-based GPR. The contributions of the work outlined in the thesis are meant to make the GPR lightweight and easily usable from the drone platform such that there is little intervention on behalf of the researcher as well as has peripherals in place to help mitigate intrinsic issues of UAS-based radar such as altitude instability.

The novelty of the UAS-based scatterometer is that it is also implemented from a drone, but for ease of mobility of the radar to better image a large area of land compared to traditional ground-based scatterometers that can take a considerable amount of time and effort to image large areas. With the drone implementation, the scatterometer can image a large field quickly. The contribution of the UAS-based scatterometer outlined in this thesis, similar to the UAS-based GPR, is to be light weight and easily usable such that data collection is not difficult for the researcher. Another

contribution for this system is its ability to switch the radar polarization during flight without intervention of the researcher.

The novelty of the ground-based scatterometer is to be a truth-basis for the UAS-based scatterometer. There is a need for a traditional ground-based scatterometer that operates with good accuracy to compare to the experimental data of the UAS-based approach to determine what, if any, intrinsic issues and noise are in the UAS-based scatterometer data caused simply by its implementation from a drone. The contributions outlined in this thesis are to make a ground-based scatterometer that is highly mobile and maneuverable in the field. This approach intends to make the payload both light weight but also durable and robust to ensure it can be used to image a large area quickly in multiple places compared to the other ground-based scatterometers using utility trucks, large boom-lifts, and large static structures and towers.

1.4 Outline of Thesis

This thesis is divided into five subsequent chapters. Chapter 2 presents the necessary technological background and theory for the development of the research discussed in this thesis. Chapter 3 introduces the approach and implementation of the UAS-based GPR. The approach and implementation of both the ground-based and UAS-based scatterometers is introduced in Chapter 4. Chapter 5 outlines the results of data collection for both the GPR and scatterometer systems. Chapter 6 outlines the conclusion of the thesis and offers means of improvement to the GPR and scatterometer systems for future efforts.

CHAPTER II

BACKGROUND

This chapter serves to provide the underlying theory and intuition necessary for the prescribed results within this thesis. The traditional methods of application and terminology for microwave remote sensing is given in Section 2.1. Scatterers including point, discrete, and distributed targets are explained in Section 2.2. Background on ground penetrating radar and scatterometers are discussed in Section 2.3 and Section 2.4 respectively. Section 2.5 outlines the necessary microwave analysis theory and techniques used to measure and characterize the GPR and scatteroemeters systems. Section 2.6 illustrates the microwave components used in the development of the GPR and scatterometer systems.

2.1 Microwave Remote Sensing

Microwave remote sensing (MRS) is a class of tools that came to prominence in the 1960s for imaging and characterizing the environment using electromagnetic (EM) energy in the microwave region between 300MHz-300GHz [30]. Before this time, environmental optical sensing, such as aerial photography, was the major method for characterizing our environment in lieu of in situ measurements in the field. This greatly increased the present sensing capabilities by introducing active sensing techniques as opposed to traditional passive techniques. Where environmental optical sensing relies on passive radiation from the sun, MRS can also utilize other means of

radiation such as targeted transducers or natural phenomenon like the earth. This also means that MRS can be conducted during day or night as sunlight is not the dominant radiation source. As MRS utilizes microwave radiation, it is able to image the environment through atmospheric conditions such as clouds, rain, fog, as well as clutter like trees and dense vegetation. This is not feasible with optical sensing because visible light is not able to penetrate these hazards and is easily scattered. At its core, there are two classes of MRS: active and passive sensors. Active sensors, known as radars, transmit microwave energy into the environment and collect the reflections of the energy off of a target. Passive sensors, known as radiometers, do not transmit their own microwave energy into the atmosphere but instead collect energy that which is already present in the environment [30].

2.2 Scatterers

In MRS theory, objects of interest that scatter incident EM energy in the environment are often referred to as scatterers or targets. Every physical material can be considered a scatterer, but the properties governing its ability to reflect, or scatter, EM energy depend on a number of factors including density, chemical makeup, size, and shape.

The adopted method of characterizing the performance of a radar is given by the radar range equation, shown in equation 2.1. This equation encompasses the fundamental phenomenon governing the propagation of EM energy through space and the resulting energy reflected off of a target to yield the returned energy back at the radar. The parameters that influence the equation are the transmit power P_t, the antenna gain G for a monostatic system, the wavelength of the EM wave λ which is the speed of light c divided the frequency f of the EM wave, the radar cross section

(RCS) σ of the target assuming a point like target, and the distance between the antenna and target R.

$$P_r = \frac{P_t G^2 \lambda^2 \sigma}{(4\pi)^3 R^4} \tag{2.1}$$

2.2.1 Point and Discrete Targets

The simplest scatterer is a point target. This is a theoretical target whose RCS is uniform across all aspect angles. The RCS of an object describes its effective area and size for which incident EM energy can reflect off of the object back to a radar receiver. In non-ideal targets, also known as discrete targets, this is not a uniform attribute of a target and varies with the radar's perspective of the object. This attribute is also a function of frequency and polarization. Idealized point targets with known RCS values are presented below. These values are important as they represent the observed targets used in characterizing the performance of both the GPR and the scatterometers.

Table 2.1

Radar Cross Section for idealized circular plate, square plate, and dihedral reflector

Circular plate, radius = a	$\frac{4\pi^3 a^4}{\lambda^2}$
Square plate, side length = a	$\frac{4\pi a^4}{\lambda^2}$
Dihedral reflector, side length = a	$\frac{8\pi a^4}{\lambda^2}$

2.2.2 Distributed Targets

Distributed targets, also known as volume targets, build upon the base theory of point and discrete targets. In a real-world environment, there are multiple targets occupying the volume or area that the antenna's beam pattern is capable of illuminating. The targets in the volume or surface

have differential RCS components and as such need to be averaged across the resolution cell of the antenna. For this, the generalized radar range equation is used which has a differential RCS that changes with azimuth Θ and elevation Φ and a differential power density that changes with azimuth and elevation. The received power response and losses are then integrated over the volume of the resolution cell shown in Equation 2.2 where L_s and L_a account for system and atmospheric losses respectively [8] [25].

$$P_r = \frac{P_t \lambda^2}{(4\pi)^3 L_s} \int_{\Delta V(R_0,\Theta_0,\Phi_0)} \frac{P^2(\Theta,\Phi)}{R^4 L_a(R)} \, d\sigma(R,\Theta,\Phi) \tag{2.2}$$

2.2.3 Polarization

EM energy as it propagates through a medium is built fundamentally by two fields known as the electric field $\hat{E}$ and magnetic field $\hat{B}$. These fields, governed by Maxwell's equations, are prescribed to be orthogonal to one another. For example, given a $\hat{E}$ field in the xy-plane, the $\hat{B}$ field will occupy the xz-plane while the energy propagation direction, in accordance with Poynting's vector, $\hat{E} \times \hat{B}$ ($\frac{1}{\mu_0}$), will move in the $\hat{x}$ direction. This property of EM fields is known as polarization and is generally described with respect to the orientation of the electric field. When the energy is incident on a target, the resulting reflection will flip the electric field across its axis in the xy-plane but maintain the field's plane of oscillation.

Antennas hold a unique property as a transducer of EM energy in that most antennas have reciprocity. This means that an antenna's ability to transmit an EM field with a given electric field orientation also makes it susceptible to receive EM radiation in the same electric field orientation. Thus, an EM wave incident on an antenna with its electric field oriented orthogonal to that of the antenna's susceptibility of an electric field will not be transduced.

Antenna polarization is then useful in observing target returns where the expected EM energy incident back to the radar is no longer in the same polarization as the transmitted energy's polarization. Radars that have two antennas can hold different polarization configurations. The first polarization is known as co-polarization where the two antennas are oriented with their electric fields in the same plane, either Vertical-Vertical or Horizontal-Horizontal orientation. The second polarization is known as cross-polarization where the two antennas are oriented 90° from one another, either Vertical-Horizontal or Horizontal-Vertical orientation.

2.3 Ground Penetrating Radar

Ground penetrating radar (GPR) is an application of radar technology with a purpose, as its name implies, to characterize targets of interest (ToI) below the ground or behind a surface. GPR is applicable in many disciplines with many examples of targets such a pipes and conduit mapped for civil and structural engineers, artifacts found in archaeological excavation sights, and landmines in foreign areas imaged in defense of military efforts. This is done by measuring the EM energy that reflects from them below a surface.

At its basis, GPR sends an EM wave from above the surface into the surface. When the wave is incident on the surface, two phenomena occurs. It will reflect off of the surface in some proportion and it will penetrate the surface and continue traveling through it in a complimentary proportion. If there is a ToI below the surface, it will have a different electric permittivity, magnetic permeability, and conductivity than that of the surrounding medium. The EM energy will reflect off of the ToI and propagate a portion of the energy back to the radar according to its RCS. This sequence of

events take a measurable amount of time and this time can be leveraged to characterize the depth of the ToI.

The EM energy transmitted in the GPR developed in this thesis spans a wide bandwidth of frequencies. As the frequency of operation increases, the spatial resolution for imaging the TOI gets better but the depth of detection below the surface gets worse. Frequency bands in the low Megahertz range can penetrate the subsurface of more than 30 meters [3]. At higher frequencies between 300MHz to 3GHz, GPR can image below the subsurface at roughly 1 meter with higher spatial resolution.

GPR can be built around either pulsed radar or continuous-wave (CW) radar. In pulsed radar, a series of short high-energy EM pulses are emitted and their echos off the ToI is measured. In the CW-based GPR, an EM wave of a specified frequency is transmitted and the receiver listens for its reflection off of a target. If the frequency of operation for CW radar changes over a specified amount of time, it is known as a frequency-modulated continuous wave (FMCW). If the frequency changes linearly over time, this is known a linear frequency modulation (LFM) waveform or "chirp" signal. If the frequency of operation changes in finite increments and in stages over time, this is known as a stepped-frequency continuous wave (SFCW) [11].

In a SFCW-based GPR, the radar sends out the signal with a specified bandwidth and number of points, or frequencies, within the signal. The reflection of one scan from the GPR, that is transformed from the frequency domain to the time domain, is known as an A-scan. The A-scan is a one-dimensional signal that when plotted, has its x-axis as time and its y-axis as the voltage of the reflection. When the GPR collects multiple spatial scans, they can be gathered together to form a B-scan. A B-scan is a two-dimensional image where the x axis denotes the number of the scan,

the y-axis denotes the time of the signal, and the voltage of the reflection is given as a gradient heat-map on the image in lieu of a third dimension for the graph [3]. The resulting image appears as a cross-sectional view of the ground surface over a the distance traversed by the GPR, illustrated in Figure 2.1. The target response will appear as a hyperbolic response on the B-scan image. This is due to the antenna radiation pattern interacting with the target incrementally as the GPR moves across the ground surface. When the GPR is directly above the target, the greatest reflection will be measured and can be illustrated in the B-scan in Figure 2.1.

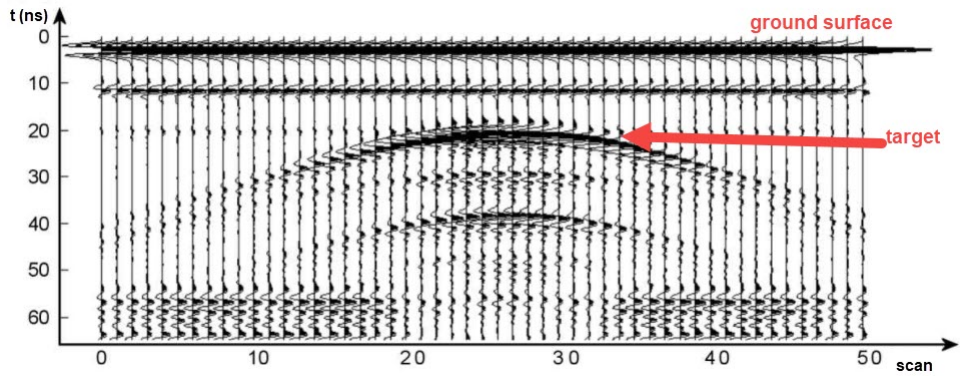

Figure 2.1

GPR B-Scan Example [3]

2.4 Scatterometers

Scatterometers are a radar-based technology used to characterize a surface by measuring EM energy scattered from surface reflections. Traditional radar operates on point, or rather discrete, targets while scatterometers are focused on distributed targets. Many scatterometers into the mid 1980s were magnitude-only scatterometers where no phase information is needed for processing. Since then, scatterometer technologies have moved toward polarimetric radar. Polarimetric radar for scatterometers is useful for collecting scattering coefficients for any number of targets [26].

Polarimetric radar is concerned with characterizing a target(s) using EM waves transmitted in multiple polarizations, namely vertical and horizontal polarization, along with using antennas of different polarization for receiving the return signal. Polarimetric scatterometers are limited by three major factors for detection when measuring targets with small RCS. The first factor is the minimum noise level of the radar system which is determined by the thermal noise level of the system. This second factor is the dynamic range of the system which is important in radar systems with one antenna or poor isolation between the transmit and receive chain of the radar. The third factor and most prominent reason for poor target detection is internal reflections that cause noise in the target range. The RF circuit and components of the radar, if not perfectly matched, create reflections of varying time delays and cause standing waves within the circuit that distort the echo response from the target. This factor is best resolved with radar calibration techniques which can map the noise from internal reflections and they can be accounted for in processing of the target returns [26].

2.5 Microwave Analyzers

In this section we describes the theory of microwave analysis including networks and scattering parameters.

2.5.1 Microwave Networks

A grouping of electrical components that are connected together in a closed loop to act on the flow of electrical current is known as an electrical circuit. When these electrical components operate at frequencies in the microwave region of the EM spectrum, namely 300MHz-300GHz, the electrical circuit is known as microwave network. Given the currents and voltages in a network are alternating, they are characterized by both their magnitudes and phases, represented as a vectors. Built from these ideas, the analysis of microwave networks is known a vector network analysis. The primary goal of vector network analysis is to characterize the flow of energy through various components to best understand the power response and loss across a network.

2.5.2 Scattering Parameters

Vector network analysis is concerned with measuring the amount of energy that propagates into and away from microwave components in the microwave network. A device that can perform this analysis is known as a vector network analyzer (VNA). Traditional VNAs have both transmit and receive ports that are used to send a microwave signals with well defined characteristics to a device under test (DUT) that can be measured at the receive port to characterize the DUT. The scattering of energy through a DUT can be defined by four parameters (S_{11}, S_{21}, S_{12}, S_{22}) known as scattering parameters. These scattering parameters are illustrated in Figure 2.2.

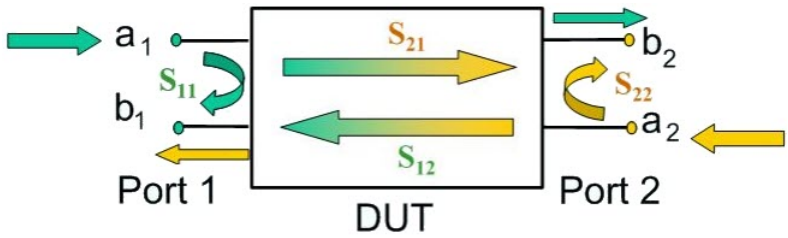

Figure 2.2

Example of a 2-port microwave network and scattering parameters [4]

In general, microwave energy that is incident on a DUT can do two things. It can propagate through the DUT and continue forward in the network, or it can experiences impedance mismatching between the transmission line and the DUT and reflect back toward the source. If the DUT is a passive microwave component, it will allow microwave energy to flow through it in both directions, called bi-directionality. VNAs use a convention to reference these scattering parameters, also known as S-parameters. The VNA will transmit energy from its Port 1. The first S-parameter is known as S_{11}. This parameter denotes the ratio of the energy received at Port 1 of the VNA to the energy transmitted from Port 1 of the VNA. This parameter is used to measure reflections of microwave energy that does not propagate through a DUT and is used to understand how well two microwave components are matched, or have similar impedance, in a network. The second parameter to discuss is known S_{21}. It denotes the ratio of energy received at Port 2 of the VNA to the energy that is transmitted from Port 1 of the VNA. This parameter is used to measure how much energy propagates through a DUT. As many passive microwave components are bi-directional, a VNA can also test a DUT's tendency to transmit and reflect incident energy that originates from Port 2 instead of Port 1. Similar to S_{11}, the third parameter known as S_{22} measures the reflected

energy toward Port 2 that originated from Port 2. The final parameter, similar to S_{21}, is S_{12} which measures the energy that propagated through the DUT at Port 1 that originated at Port 2. Built from available S-parameters, there are characteristics of a DUT that are useful. The first characteristic is known as Insertion Loss. This term refers to the amount of energy that a passive microwave components attenuates from acting on the energy and is given as $|S_{21}|$. In general, the lower this value is, the better. The next characteristic is known as Return Loss. This term refers to the amount of power that will reflect back from a DUT to the source. It is relative to the incident energy on the DUT. In general, the higher this value is, the better performance a DUT has and is given as $-S_{11}$. Return loss is also known as a components directivity where the value denotes the how much energy will propagate into a DUT compared to the amount of energy that will be reflected.

2.6 Microwave Components

There a many different types of microwave components that can be used in a network. In general, all components can be categorized into one of two groups, active components or passive components. Active components act on microwave energy in tandem with an outside power source to alter the amount of power that transmits out of a microwave component. Examples of these components are microwave amplifiers and microwave switches. Microwave switches are used to change the propagation path of a network using logic controls from devices such as micro-controllers and mechanical switches.

Microwave amplifiers are one of the most well known active microwave components used in networks. The purpose of amplifiers is to increase the signal power of the energy that enters them by a specified amount, known as gain. This is done with the intent of preserving the intricacies

of the signal and only increasing its maximum amplitude. The are a number of factors regarding amplifiers that characterize their performance. The first factor is known as the amplifiers Noise Figure. For any signal, there is an underlying minimum level of noise associated with the signal's frequency spectrum. The difference in signal power and noise power is defined as the Signal-to-Noise Ratio (SNR). The higher the SNR, the easier it is to detect a target. When using a microwave amplifier, the Noise Figure denotes the decrease in the signals SNR after amplification. The lower the Noise Figure an amplifier has, the better it will maintain the original signal's SNR after amplification.

The next factor of a microwave amplifier is its 1dB compression point (P1dB). In general, amplifiers are designed to linearly increase a signal's power by a static gain. For a given amplifier gain, the amplifier is designed to be able to increase the original signal's power by the gain regardless of the original signal's input power level. As amplifiers are not ideal devices, there is an input power level where the amplifier is no longer able to increase input signal's power level by the rated gain. There is also a point in all amplifiers where no matter how much input power is injected into the amplifier, the amplifier will no longer increase the output power. The point where the difference between two output power's from an amplifier is less than 1dB is known as the amplifiers 1dB compression point, illustrated in Figure 2.3. This is considered to be an amplifier's maximum output level before potential damage to the amplifier from too much input power.

Passive components do not rely on an outside power source and only act on the incident microwave energy to modify the signal. Examples of these devices are attenuators, antennas, isolators, circulators, and directional couplers.

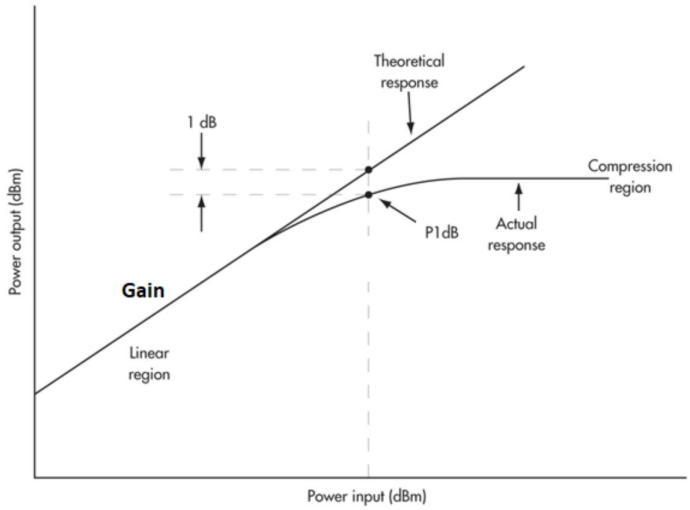

Figure 2.3

Point of 1 dB compression (P1dB) graph [2]

Attenuators are components that are used to degrade the forward power from a source power by a precise amount. This helpful when wanting to limit the power incident on microwave components that have specific input power constraints. The next component is an antenna. Antennas are transducers which are devices that can convert energy from one state to another. In this application, antennas convert bounded EM energy to an unbounded form that can propagate through the air and the environment.

The next component is known as an isolator. An isolator is a component that limits the energy flow to one direction through a network. This device is useful when separating the transmit and receive chains for a radar system where high power reflections caused from impedance mismatch could damage the transmit and receive chains.

The next component is a circulator, shown in Figure 2.4. This is a multiple port device that leverages uni-directionality to only allow energy transmitted into one port to exit a single, separate

port. Circulators build upon on the idea of the isolator and can be used to isolate the transmit and receive chains of a radar so that an antenna can transmit and receive microwave energy while not directly passing the energy between the two chains.

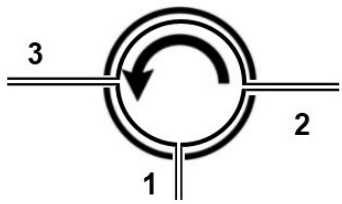

Figure 2.4

Circulator

The last passive component is known as a directional coupler. A directional couplers, show in Figure 2.5, is a device that samples a signal at a fraction of a incident power by leveraging the direct coupling between two transmission lines that are close together. There are the three accessible ports on a directional coupler with a four port connected to a 50-Ohm load. The IN port (port 1) and OUT port (port 2) of the directional coupler is a transmission line. The coupled port, CPL, (port 3) the load port (port 4) are also connected with a transmission line. With the fourth port loaded, the CPL and IN port are connected via coupling to act as a transmission line with a predefined coupling loss. Because of the loaded port, the coupling primarily occurs between the IN and CPL ports with little interaction between the CPL and OUT ports. This amount of power is denoted by the directional coupler's directivity. The isolation of the CPL and OUT ports is found by subtracting the coupling loss from the negative of the directivity.

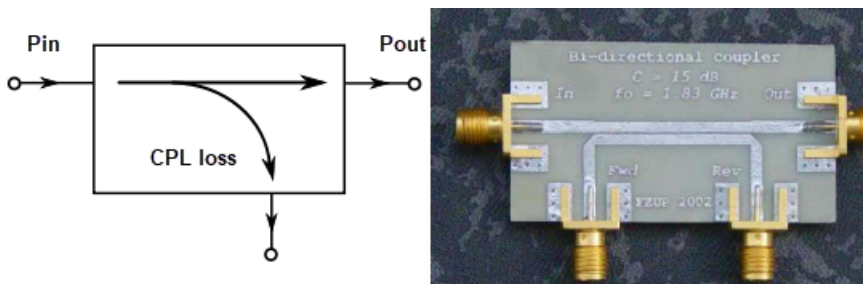

Figure 2.5

(a) Circuit diagram of a (b) directional coupler [1]

CHAPTER III

GROUND PENETRATING RADAR

3.1 Approach

In this chapter we introduce the general approach and system for the developed UAS-based GPR system. The objective of designing a UAS-based GPR is to mitigate some of the issues that are present in ground-based GPR. This means the GPR must not introduce other systemic issues that nullify the need for the UAS-based approach for lack of substantial benefit. The GPR needs to be able to collect scans of data quickly given the traveling speed of the UAS in order to sample the ground in small spatial increments. It should be a light weight system suitable to be carried with a small or medium-sized drone that can fly at least 10-15 minutes. The GPR must have peripherals to track the height of the system to account for variance in the UAS flight height. The system must also be able track global positioning system (GPS) information for connecting the radar returns and target detection with a point in space. Lastly as verification, the system must obtain visual confirmation that the GPR is flying over an area suspected to have a target.

3.1.1 System Overview

The developed GPR system is controlled with an Intel Nuc mini-pc which runs a Windows operating system and is the brain of the system. The GPR uses the UVNA-63 transceiver and RFSPACE Vivaldi antennas for the basis of the radar.There are also other peripherals including a

USB camera, Arduino Mega 2560, and TF-Mini Lidar. The computer, transceiver, and all other peripherals are powered with a POWERADD variable battery bank. The mini-pc is powered with 19V and the other devices are powered with 5V from the mini-pc.

3.1.1.1 UAS

As the novelty of this GPR is its application for UAS, the first subsystem is the UAS, shown in Figure 3.1. The UAS utilized for this GPR is custom-built by the IMPRESS Lab, using commercially available carbon fiber frames, DC brushless motors, flight controllers, and real-time kinematic (RTK) sensors. The brands and models of the components are inconsequential, rather the operating parameters of the UAS and constraints are worth noting.

Figure 3.1

UAS-based GPR flying

Table 3.1

UAS flight constraints for GPR payload

Flight Time	Maximum Flight Speed	Maximum Payload Weight	Maximum UAS Weight
15 min	5 m/s	6 lb	22 lb

From Table 3.1, the main attribute of the UAS constraints for the GPR is the maximum payload weight. At 6lbs, this allows for the weight of the UAS with the payload attached to be 5lb less than the maximum rated load. The GPR, encompassing a transmitter, computer, antennas, the frame holding the GPR, and other peripherals needs to be light weight.

3.1.1.2 UVNA-63

As described in the literature from Chapter 2 Section 3, there are a number of methods of transmission for GPR applications ranging from impulsed radar to frequency modulated continuous wave (FMCW) radar as well as stepped frequency continuous wave (SFCW) radar. For its ability to scan a large bandwidth, a Vector Network Analyzer (VNA) is used as the GPR's transmitter. The UVNA-63, shown in Figure 3.2, is an experimental, programmable VNA developed by Mini-Circuits in partnership with Vayyar [5]. While it is capable of operating as a high-fidelity VNA, it functions well as a SFCW transceiver weighing less than 1lb and is leveraged for the GPR in this application. It has an operating band of 100MHz-6000MHz. The use of the SFCW signal will ensure adequate range resolution given its ability to transmit in a large bandwidth.

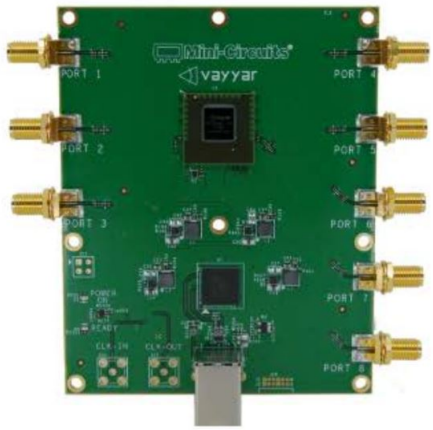

Figure 3.2

Mini-Circuits UVNA-63

3.1.1.3 Vivaldi Antennas

The next aspect of the GPR to consider are the antennas. The UVNA-63 used in the GPR is equipped with multiple transmit and receive ports. This is allows the system to be leveraged with two antennas, one for transmit (TX) and for receive (RX), which mitigates the need for oscillators and other RF components while still being a mono-static radar with the close proximity of the two antennas. The antennas for this GPR need to have a wide bandwidth and be light weight given the weigh constraints of the UAS. For these reasons, RFSPACE Ultra Wide Band (UWB) Vivaldi antennas were selected for the GPR, shown in Figure 3.3. The antennas are placed 20.7cm apart when equipped to the drone and are capable of transmitting between 800MHz-6000MHz with an S_{11} response of less than -10 dB across the band.

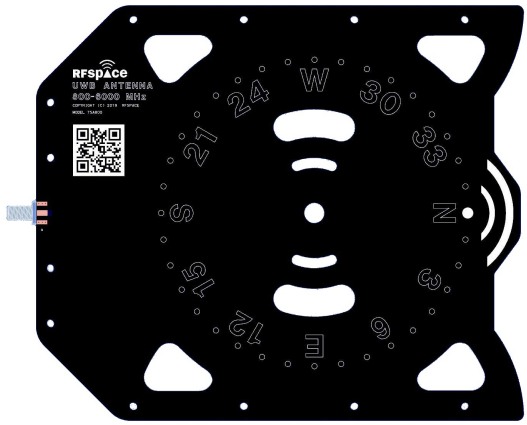

Figure 3.3

RFSpace UWB Vivaldi antenna

The manufacturer calculated the peak gain of the antennas at various points across the band, shown in Table 3.2. Additional to the antenna gain measurements, the manufacture also generated antenna beam patterns across the band for 800, 1000, 2000, 3000, 4000, and 5000 MHz, shown in Figure 3.4.

Table 3.2

Antenna gain values in dB for RFSPACE UWB Vivaldi antenna between 800-6000GHz

Frequency (MHz)	Gain (dB)	Frequency (MHz)	Gain (dB)
800	3.15	3400	9.34
1000	4.94	3600	9.04
1200	4.89	3800	9.37
1400	6.35	4000	8.60
1600	7.50	4200	8.31
1800	7.99	4400	8.19
2000	8.31	4600	8.12
2200	8.79	4800	7.97
2400	8.55	5000	7.27
2600	8.76	5200	6.82
2800	8.97	5400	7.02
3000	8.80	5800	6.08
3200	9.19	6000	7.78

3.1.1.4 GPR peripherals

It is important to know where the UAS is flying over for each scan of the GPR. To solve this, the GPR has an added camera peripheral that images the ground surface during testing. The GPR system is also equipped with an Arduino Mega 2560 to communicate with various sensors. In this application, the Arduino controls a TF-Mini Light detection and ranging (Lidar) unit. Below in Figure 3.5 is a picture of the peripherals used in the GPR system.

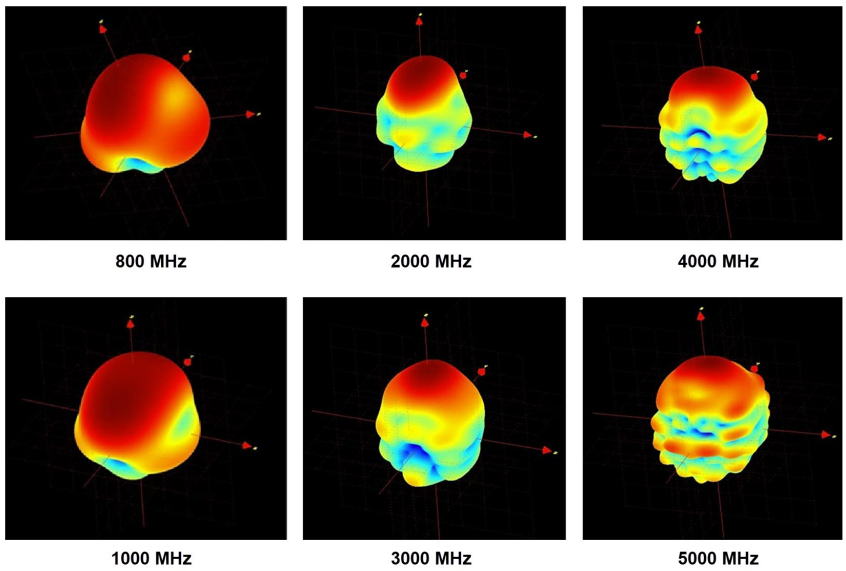

Figure 3.4

RFSpace UWB Vivaldi antenna 3D beam patterns [10]

3.1.2 Integration and Operation

The UVNA-63 can be controlled using various programming languages such as Python and MATLAB. For this application, Python 3.8 is used as it is computationally light weight and it is capable of interfacing with the peripherals in the GPR system. The camera can be controlled with the "OpenCV" package within Python to image the ground during the VNA testing. Figure 3.6 illustrates the full system and the accompanying connections between all components of the UAS based GPR.

Figure 3.5

GPR peripherals

Figure 3.7 below shows the operating parameters of the GPR. The VNA, while capable of increasing the upper limit of the band to 6000 MHz, is set to not scan above 5000 MHz. This is to mitigate the loss in beam efficiency as the beam patterns from Figure 3.4 show the side lobes power growing incrementally as the frequency increases. Through parametric testing with the number of points and the resolution bandwidth (RBW), 401 points a RBW of 21 kHz yields the fastest scan time for the GPR at approximately 33 scans per second. The GPR's operating parameters are listed Table 3.3.

With the use of the VNA's proprietary communication protocols, the Arduino and LIDAR unit's serial communication, camera's USB communication, it is important to be able to make the GPR system easily usable. The first step to achieve this is to make simple graphical interface (GUI) from the base code for the system. Using the "Tkinter" package in Python, the GUI shown in Figure 3.7 is created. The GUI allows for changes to the VNA parameters. Once the desired values are selected, the VNA begins to run. For every 5 scans of the VNA, the program uses the

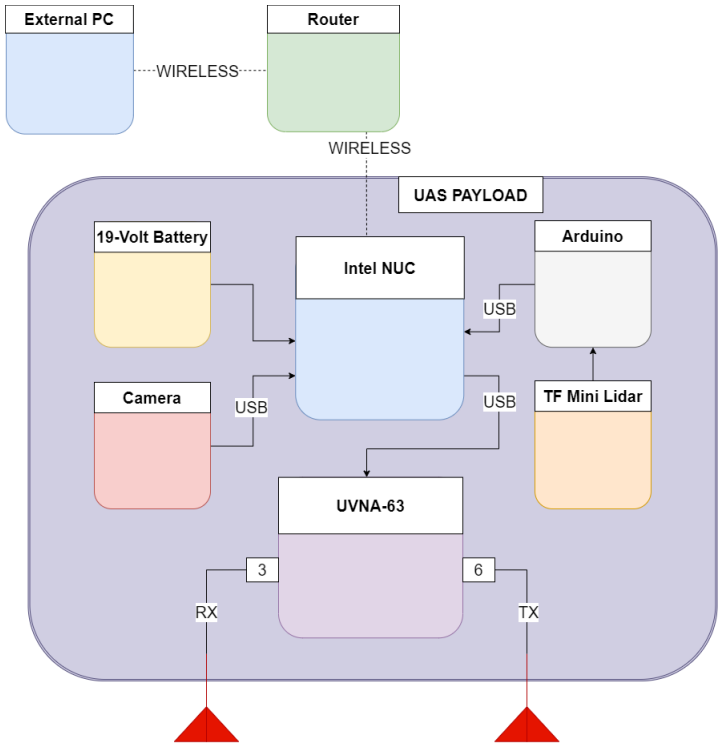

Figure 3.6

GPR systems schematic

camera to take an image of the ground below the UAS. Additional to the camera, for every 5 scans of the VNA, the program communicates with the Arduino to collect a single data point from the Lidar unit.

The python programming running the GPR's software is highly dependent on specific packages and files to work. The program can not be put on another machine without significant work being done to ensure the computer handles the commands in a correct manner. To avoid this, the python code and its GUI are packaged into a distributable executable file (.exe) that encompasses everything needed to run the GPR. With this approach the software can be opened on any computer

Table 3.3

GPR system operating parameters preallocated in GUI for field testing

Start Frequency	Stop Frequency	Points	Resolution Bandwidth	Power Level
800 MHz	5000 MHz	401	21 kHz	0 dBm

system with virtually no setup and with the correct devices connected to the computer, the GPR will work as intended.

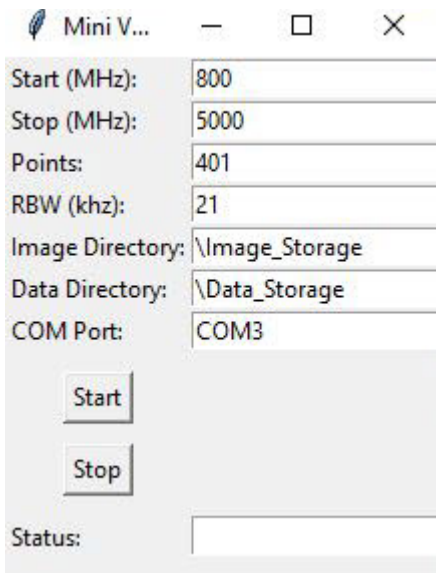

Figure 3.7

GPR Python-based GUI

3.1.3 3D Printed Carriage

To house the GPR, a number of 3D printed boxes were developed. 3D printing enabled the GPR to be housed in a highly customized structure that securely holds the individual components. This mitigates the issues of vibration caused by the drone which can make cables and other connections come loose. This also has the added advantage of keeping all of the components water-tight during flight. The approach of modeling a housing and printing it from commercially available printing filaments allows the system to be made quickly, lightly, and cheaply. The GPR housing went through many iterations of creation to ensure the best fit and the final housing securely holds all of the components and weighs less than 900g. The iterations of housings and final the housing can be seen in Figure 3.8.

Figure 3.8

(a) all iterations of the GPR 3D printed housing and (b) final iteration of GPR housing with components inside and (c) 3D printed housing mounted to the bottom of the drone

3.1.4 Ground Height Normalization

A major systemic issue to correct in the UAS-based GPR is the variance in the relative ground height. Traditional GPR systems are ground based and as such are always the same distance away from the ground. Traditional GPR sets the zero point in time to the top of the ground surface. In an idealized setting for the UAS where the ground is flat and level and the UAS does not shift in height during its testing, this can be achieved by subtracting out the data from the time domain that exists in the space between the antenna and the ground surface. The difference in the returns between the ground-based GPR and the idealized UAS-GPR response are illustrated below in Figure 3.9.

In a real world environment, the methods to simply the response from the time domain return of the radar are not as simple. In practice, the ground surface is non-homogeneous meaning the ground does not have the same dielectric properties or moisture content or physical density everywhere and the power density of the ground return is not consistent between any two points. Additionally the UAS system does not maintain a static altitude well due to wind and pilot errors. Lastly, the ground surface is not level everywhere and in most cases varies from point to point. These effects shift the relative ground height dramatically and this creates inconsistencies in interpreting the data. From this, there is a need to correct for this inconsistency and to normalize the ground height of the radar data. While radar technology is well equipped to monitor this change, the radar system used in the GPR is not best suited for this application.

The drone platform may move in the altitude dimension a considerable amount and the assistance of another sensing system is useful and needed to account for the altitude variance. The solution to the ground height normalization is the use of a Lidar unit. The TF-Mini Lidar unit [12] is capable of ranging targets as close as 0.3 m and as far away as 12 m and has a spatial resolution

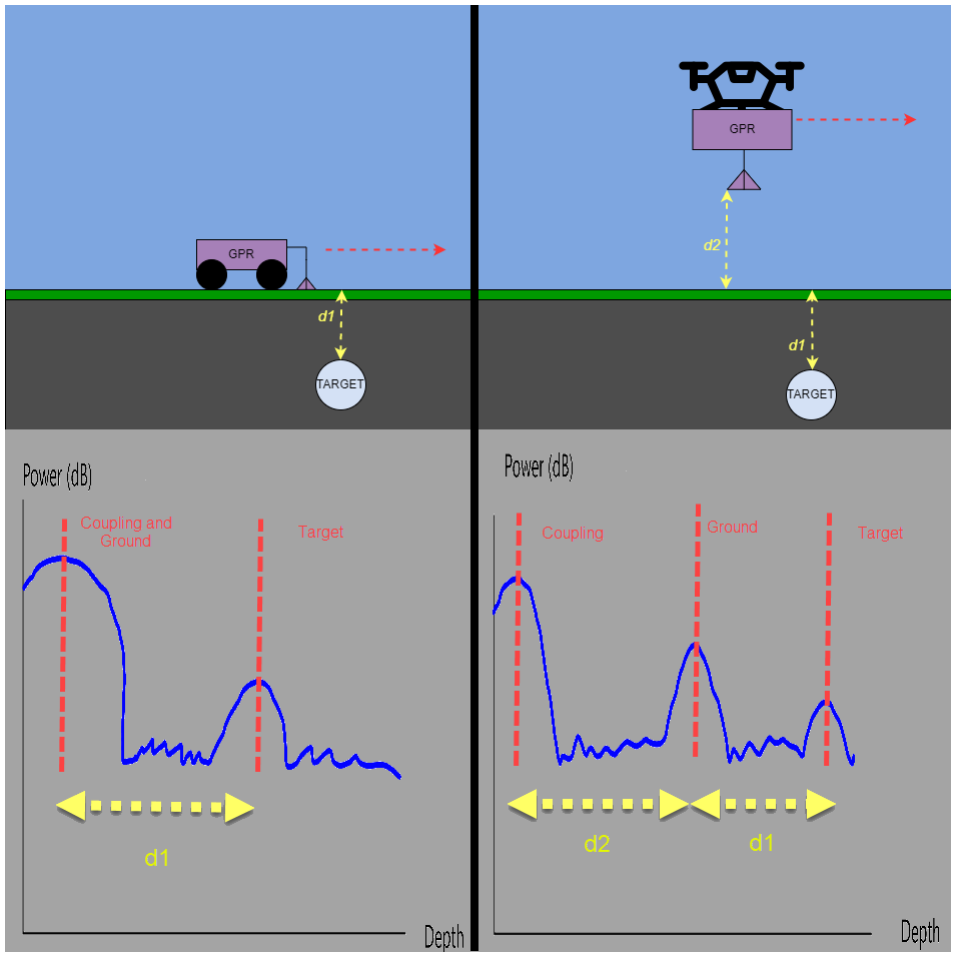

Figure 3.9

(a) Ground-based GPR response versus (b)UAS-based GPR response

of 5mm. As the transmitted energy is light, there is no concern of the energy penetrating the ground and the unit returns an integer number of the distance with accuracy within 1% of the target distance. The system is also able to sample fast at 100Hz. The Lidar unit is placed in parallel with the GPR system and does not significantly impede the collection speed of the GPR. The Lidar unit, shown in Figure 3.10, samples the distance from the GPR to the ground and the vector of data

created can be used to subtract the radar data the exists in the free space between the antennas and the ground.

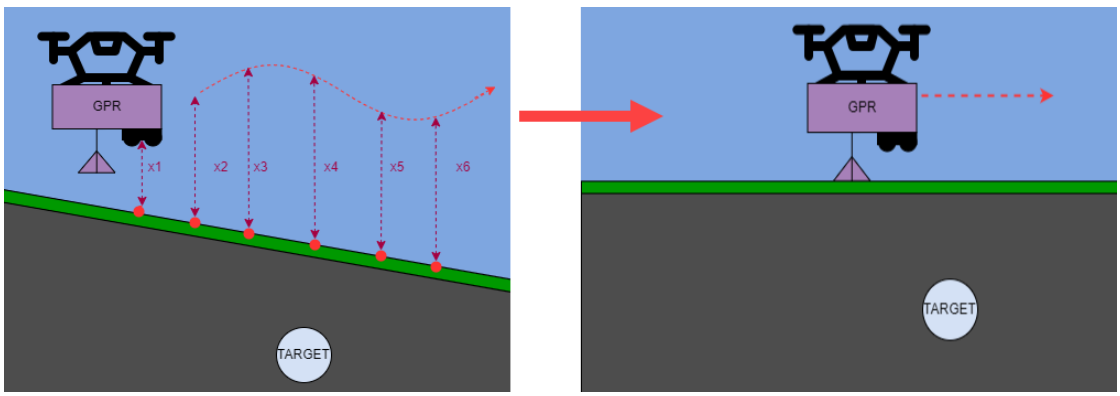

Figure 3.10

(a) GPR altitude variance and (b) LIDAR-based height normalization for GPR altitude

CHAPTER IV

SCATTEROMETER

This chapter serves to explain the development and implementation of the scatterometer system. The following illustrates the necessity of both ground and aerial based implementations and the requisite rationale for both. The development process is discussed, going over the effective design choices as well as issues found in the process.

4.1 Ground Based Approach

Before creating a UAS based scatterometer, a ground based system is needed. As a UAS based scatterometer is a new approach in the available literature, the ground based system must serve as a truth basis for data on two fronts. The ground system must demonstrate what the literature currently represents in order to characterize the ground surface with moderate fidelity and it must yield a high degree of confidence that the received data is meaningful. On a second front, the ground based system is crucial for acting as a reference system for the UAS to analyze the received data in order to adequately understand distortions in the returns caused by vibration or other forces. The ground based system, in order to approach the point where a UAS system is justifiable, must satisfy constraints that push the system to the current capabilities of a ground system. This means the ground based system must be as portable as possible which will allow the scatterometer to be used in various areas with non-ideal terrain, such as crop fields, marshy terrains, or rough and

rocky environments. The ground based system must also be capable of yielding substantial returns by scanning large swaths of area. All constraints must also push toward being done as fast and efficiently as possible. Once the best possible ground based system is created, within the bounds of both current skill and equipment availability, the overall system can be qualified for its efficiency and a UAS system can be made to address all issues stemming from the limitations of the ground based system.

4.1.1 Subsystem Overview

To address the mobility of the ground based system, the scatterometer is mounted to a HD2 Treaded ATR Tank Rover, shown in Figure 4.1. This rover is driven by two high capacity 24 volt batteries, has a free load RPM of 285, and is rated for a 100 lb load which is exceeded in this project. The extra load decreases the linear speed of the rover but does not significantly degrade the rovers torque. This makes the rover a viable option for transportation of the scatterometer. As it is equipped with all-terrain tracks, the rover can transport the scatterometer in a variety of environments including grass fields, asphalt lots, farm brush, and wet and muddy soil.

Figure 4.1

HD2 treaded ATR tank rover

To achieve a large swath area for scanning, the scatterometer must be raised to a height of at least 15 feet. Given an incident angle of 45 °, this height allows for the antenna beam pattern to have a large foot print on the area of interest. This will be achieved by mounting the system to a telescopic mast that can be electronically controlled remotely, shown in Figure 4.2. The mast is capable of raising the scatterometer 18 feet into the air which and coupled with an appropriate scan angle, will yield a sufficient field of view (FoV).

Figure 4.2

Telescopic mast

With the mobility and possible swath width of the system solidified, the means of data collection for the scatterometer must be considered. While there are a number of viable methods for creating a scatterometer, a Vector Network Analyzer (VNA) will be the transmitter for this system. This means of transmission will allow us to generate a Stepped-Frequency Continuous Wave (SFCW) signal with high precision of the desired bandwidth. As the system is meant to be truth basis for

other systems, a high fidelity VNA must be used to ensure the best possible returns. The selected system is the Keysight Agilent N9917A Microwave Analyzer, shown in Figure 4.3. This system is capable of operating as a multitude of tools including a spectrum analyzer(SA), a cable-and-antenna tester (CAT), as well as a VNA. In preparation for using a lighter weight VNA on the UAS-based scatterometer, the UVNA-63, described in Chapter 3 GPR, will again be leveraged for the ground-based system as a second means of data collection. Converse to the motivation of using the UVNA-63 with the GPR for its adequate large bandwidth response, the device also has an adequate narrow bandwidth response that is suitable for the scatterometer.

Figure 4.3

Keysight Agilent N9917A microwave analyzer

The Keysight VNA is a two port device that will transmit the SFCW signal from its Port 1. From Port 1, the energy will travel through a coaxial cable and will propagate into the air through the horn antenna rated for 1-18GHZ operation, shown in Figure 4.4. The incident energy

is reflected from the ground surface caused by any rough or non-flat target, known as backscatter, and is returned into a second and identical horn antenna and into Port 2.

The basis of the ground-based scatterometer can be seen below in Figure 4.5. These are the main components to make the scatterometer functional. From this point, the system is equipped with additional components to bring it closer to the current state of the art for a ground-based scatterometer. The final scatterometer is equipped with various attachments and subsystems in order to increase its flexibility in both data collection capabilities and robustness to face any adversities it may experience in the field.

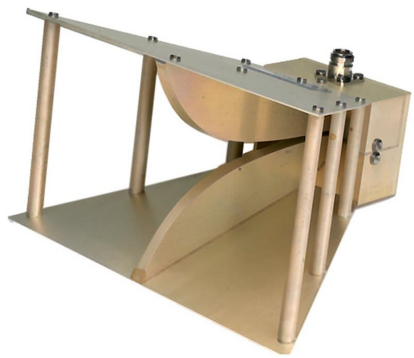

Figure 4.4

1-18GHz horn antenna

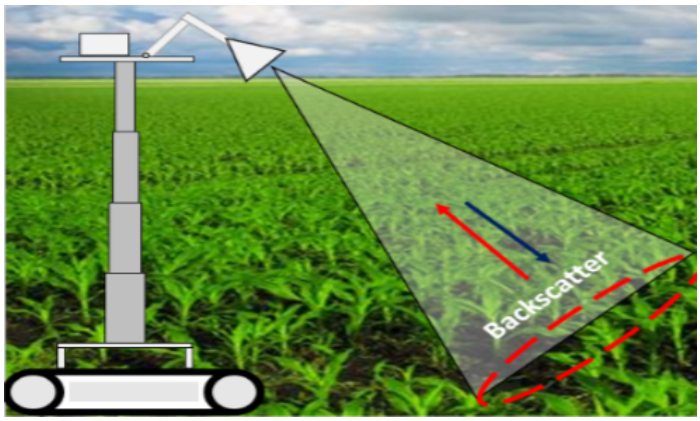

Figure 4.5

Initial ground-based scatterometer design [19]

The first subsystem to address is the variable scan angle of the antennas. As prescribed by the physics discussed in Chapter 2 Background, the antennas must be able to adapt the angle of incidence of the transmitted energy to adequately characterize the reflectively of the targets of interest (ToI) for this system (brush, crops, water, and soil) to understand properties such as crop density and moisture content. Shown in Figure 4.6, the horn antennas are mounted to two arms made of PVC pipe that are affixed to metal pipe hinges on the mast platform. This allows the antennas to propagate the incident energy with 180 ° of freedom from pointing nadir to the ground surface to point directly to the sky. The PVC pipe end has a 1/4-20 steel bolt protruding from it which is the same mounting system used by the horn antennas. The antennas are simply screwed on to the bolt until tight. This has the added benefit of allowing the antennas to be mounted in varying polarization. Since the mounting hole on the antennas is centered with the wave guide of the antenna, the rotation of the antenna matches the rotation of the antenna center point of

transmission. This mitigates coupling variance between different polarizations due to time delays cause by varying distances between the antennas.

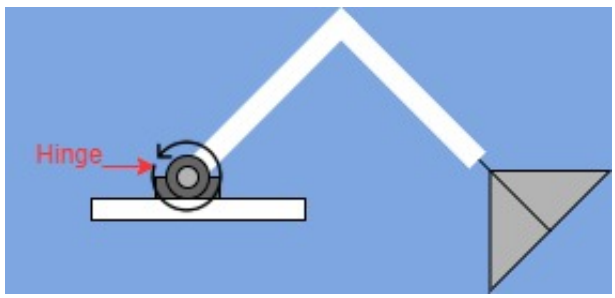

Figure 4.6

Antenna mounting structure

The next improvement made was to increase the available reach of the antenna swath width. As a stationary system suspended at the mast's maximum height, the scatterometer's available scan area is static according to position of the rover. The scannable area could be increased by rotating the antennas, shown in Figure 4.7. This increases the data's scan size in the environment being observed and yields a more averaged characterization of the geo-physical properties such as the average soil moisture and vegetation density of the area. The initial thought of simply rotating the rover to address the static swath area raised a number of problems. At its maximum heights, it would be dangerous to rotate the mast while extended. Additionally, the time to re-level the rover and re-setup the scatterometer system would be too great for a reasonable testing timeline. The solution to this problem is to not rotate the rover, but instead rotate the platform on top of the mast.

Shown in the Figure 4.8 below, a rotation platform is created to rotate the antennas while keeping the mast stationary. The main component of the rotation system is the lazy-susan base.

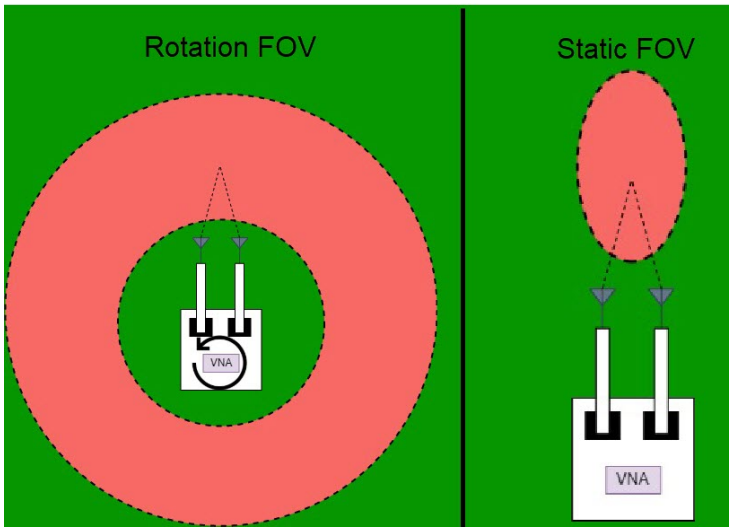

Figure 4.7

Ground-based scatterometer static FOV versus rotating FOV

This includes two rings that spin freely from one another using ball bearings. By mounting the inner ring to the mast top plate, the outer ring can freely spin and the top platform can be attached above the lazy-susan using rods placed around the outer ring. There is a center brass rod that it affixed to the top platform but free spins on the base plate. A gear is attached to the rod and is paired with a drive gear attached to a drive motor which turns the top platform. Depending on the polarity into the motor/encoder pair, the platform will rotate clockwise or counter-clockwise.

4.1.2 Integration and Operation

With the mast rotation hardware created, the next step in creating a high fidelity ground based scatterometer is to incorporate automation into the system. With the integration of automation, the scatterometer can be used with minimal user intervention and can more flexibly operate in

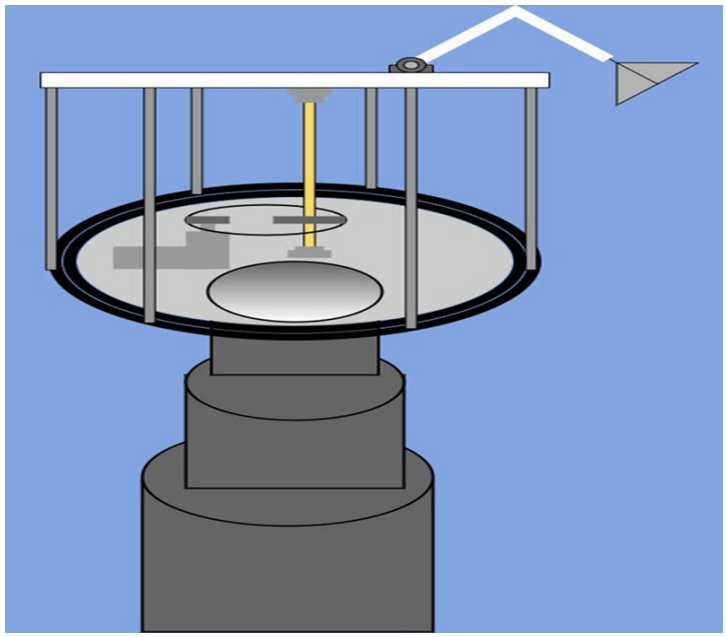

Figure 4.8

Ground-based scatterometer rotating platform

the testing environment. Figure 4.9, shown below, illustrates all of the additional subsystems incorporated into the system.

The first aspect of the system to automate is the mast control. The mast is traditionally controlled by a remote control with three switch-buttons to make the mast either move Up, move Down, or Stop movement. The solution to its automation was to solder wires to the input and output pins of the three remote buttons, totaling 6 wires, and inputting them into a control board. In this case the control board is an Arduino Mega 2560 and it is used to give remote input to control the mast's functionality.

With the mast system automated, the next point of automation is the mast rotation. The rotation motor is paired with a rotary encoder that tracks the rotational position of the platform. Connected

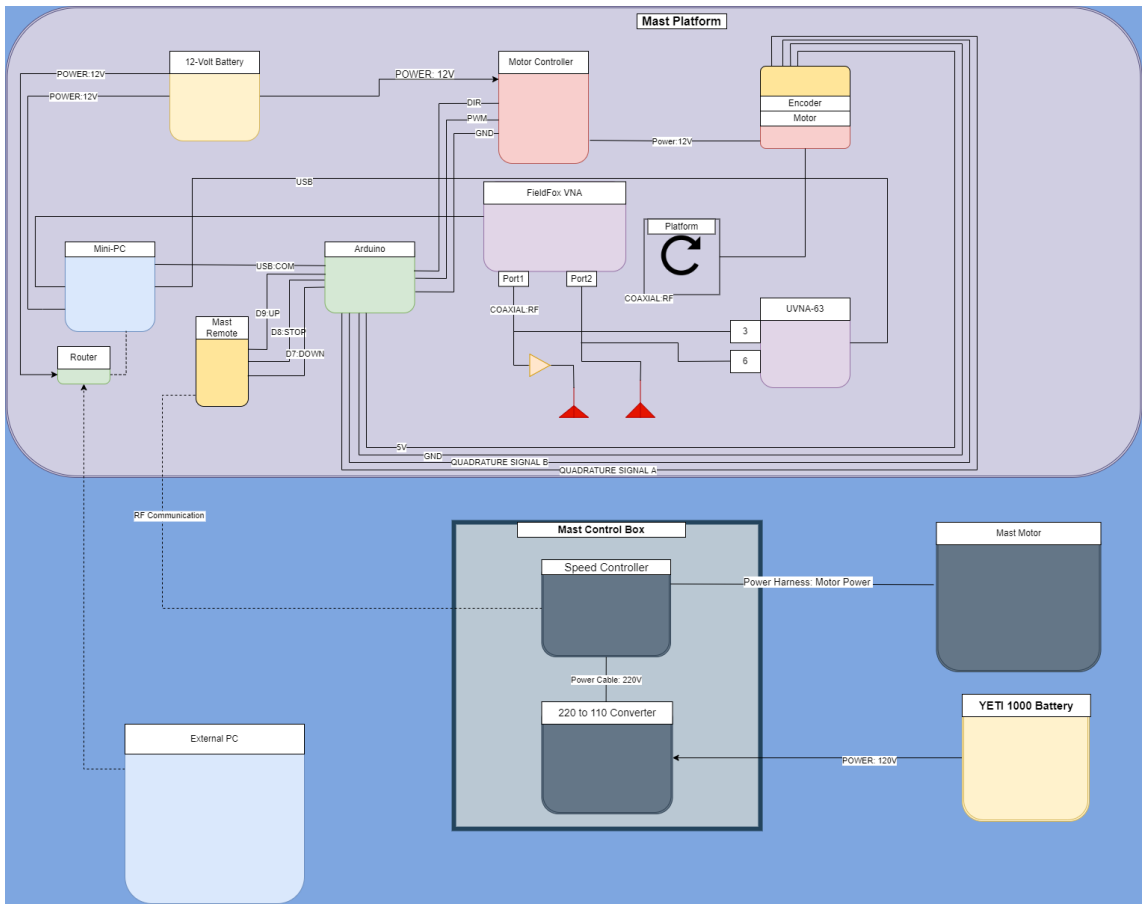

Figure 4.9

Ground-based scatterometer full system design

to the motor is a Cytron RB-Cyt-133 motor controller that it capable of both generating a Pulse Width Modulation (PWM) signal which can vary the speed of the platform rotation, and switching the polarity of the motor power which change the direction of rotation of the platform. The motor controller and the rotary encoder are both controlled with the Arduino Mega 2560 to intelligently rotate the platform with a high level of precision.

In order to control the Arduino as well as the VNAs, a Mini-PC is placed in the "Mast Control Box" that runs Windows 10. The next step is to communicate with the VNAs autonomously. Both VNAs have protocols to be controlled remotely from a computer using computer programming languages and techniques. The Keysight Agilent system utilizes a number of protocols, but for this system, the Scientific Computer Programming Interface (SCPI) commands are used. The Mini-Circuits VNA leverages it own proprietary protocols developed by the manufacturer that can also be used in programming languages.

The MATLAB software is designed for mathematical modeling and simulation and is used as the means of programming all of the subsystems in the ground based scatterometer. It has pre-built frameworks for handling both SCPI and Arduino commands. Both the Keysight Agilent VNA and Mini-circuits VNA can be controlled using MATLAB. It also has a tool called "AppDesigner" which allows users to seamlessly create Graphical User Interfaces (GUI) to better communicate with custom designed programs. Shown below in Figure 4.10 is the GUI used to control the ground based scatterometer.

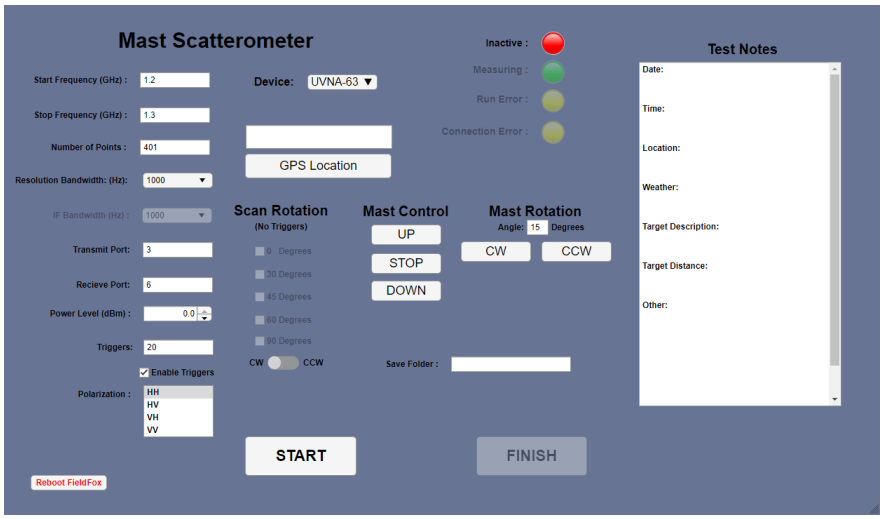

Figure 4.10

Ground-based scatterometer MATLAB GUI

The GUI is capable of controlling multiple of parameters within the system. At its core, it is capable of communicating with both VNAs and initiating testing for both with parameters such as the bandwidth, number of points, power level, resolution bandwidth (RBW) and intermediate frequency (IF).

The system can also determine how many instances of the VNA need to be scanned (known as triggers). The GUI allows the user to choose a finite number of triggers or choose to trigger indefinitely until stopped by using the "Stop" button. Additionally, leveraging the the rotation capabilities, the user can choose to trigger and rotate at the same time and scan a large swath width depending on a selected azimuth angle. In this mode, the VNA will begin triggering and the platform will begin to rotate slowly. Once the system has reached it selected scan angle, the platform will stop rotating and the VNA will stop calling triggers.

There are additional features in the GUI past the necessities of the system. When using the Keysight Agilent system, the GPS coordinates of the system can be found for noting in a report. There is also a "Test Notes" section that will document any information the users deems pertinent to the test and will save a notes file every time a test is performed. Lastly, there is a "Mast Rotation" section that allows the user to rotate the platform in order to line up the antennas while already up in the air.

System Parameters

The scatterometer is designed to have a wide range of variability for input parameters for the bandwidth, power level, and RBW. For this system, there are standard values put in place for operation of the system, listed below.

Table 4.1

Testing Parameters

Start Frequency	Stop Frequency	Points	RBW	IF	Power Level
1.2 GHz	1.3 GHz	401	1kHz	1kHz	0dBm

4.2 UAS Based Approach

This section describes the design and development of the UAS-based scatterometer including the subsystem overview and system integration.

4.2.1 Subsystem Overview

The UAS-based scatterometer is effectively the same system as the ground based scatterometer. The radar will also use the Mini-Circuits UVNA-63 as its transceiver and the post-processing algorithms for interpreting the received data will be the same. It is from this point, however, that the system deviates in its implementation on the ground-based system. This is due to the lack of in situ configuration of the antennas during testing.

The ground-based system has two 1-18GHz horn antennas as its transducers. These antennas are heavy and robust which is acceptable for the ground-based system but would be inefficient to attach to the UAS as the UAS battery would deplete much faster under the extra weight. This leads to an issue with configuring the polarization of the radar during flight testing. The UVNA-63 transceiver can only transmit out of one port at a time and currently only receives returns in one port, different from the transmit port.

The development and implementation of patch antennas for this system is the optimal solution for the UAS-based approach. This works to mitigate the weight issues of the antennas as well as meet the radar's need of high antenna gain and a large beam width for characterizing the ground from the heights of the UAS. The antennas, shown in Figure 4.11, are designed using the ANSYS HFSS antenna design software.

The antennas were designed as a joint effort with Md Mehedi Farhad for use on the UAS payload. The antennas have an average gain of 12.13dB in the main-lobe. The antennas far-field beam-pattern and S_{11} response are shown in Figure 4.12. By using two of the antennas, rotated 90° apart, both vertical and horizontal polarization is achieved.

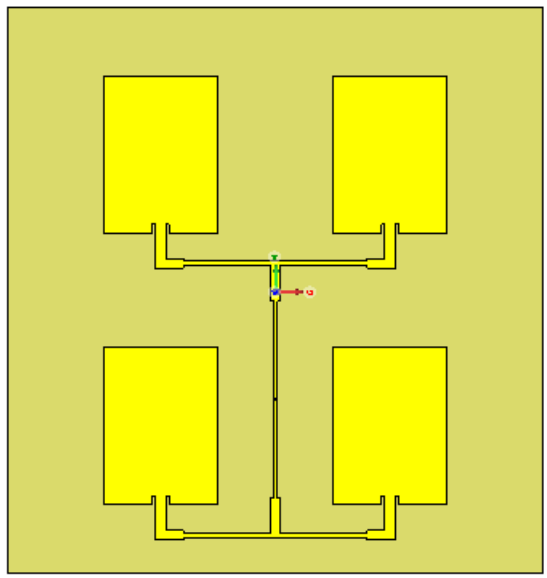

Figure 4.11

Radar patch antenna computer model

The patch antennas are fabricated by a third party and take a considerable amount of time to be delivered. As the system needs to be viable and usable before the patch antennas arrive, alternative antennas are used in the UAS-based approach. The antennas used for the initial testing of the scatterometer are ultra wide-band Vivaldi antennas from RF space. The antennas for the UAS-based scatterometer are side-looking antennas at 45° from nadir to the ground surface. To achieve this need, a structure was modeled and created in the lab's 3D printer. The model for the structure along with the fabricated structure with the antennas attached is shown in Figure 4.13.

The use of dedicated horizontal and vertical antennas leads to the biggest difference in the development of the two scatterometers. In the ground-based approach, the two horn antennas could be rotated manually during testing by raising and lowering the mast to create the four polarizations for the radar. This was possible because the ground-based scatterometer's and aspect

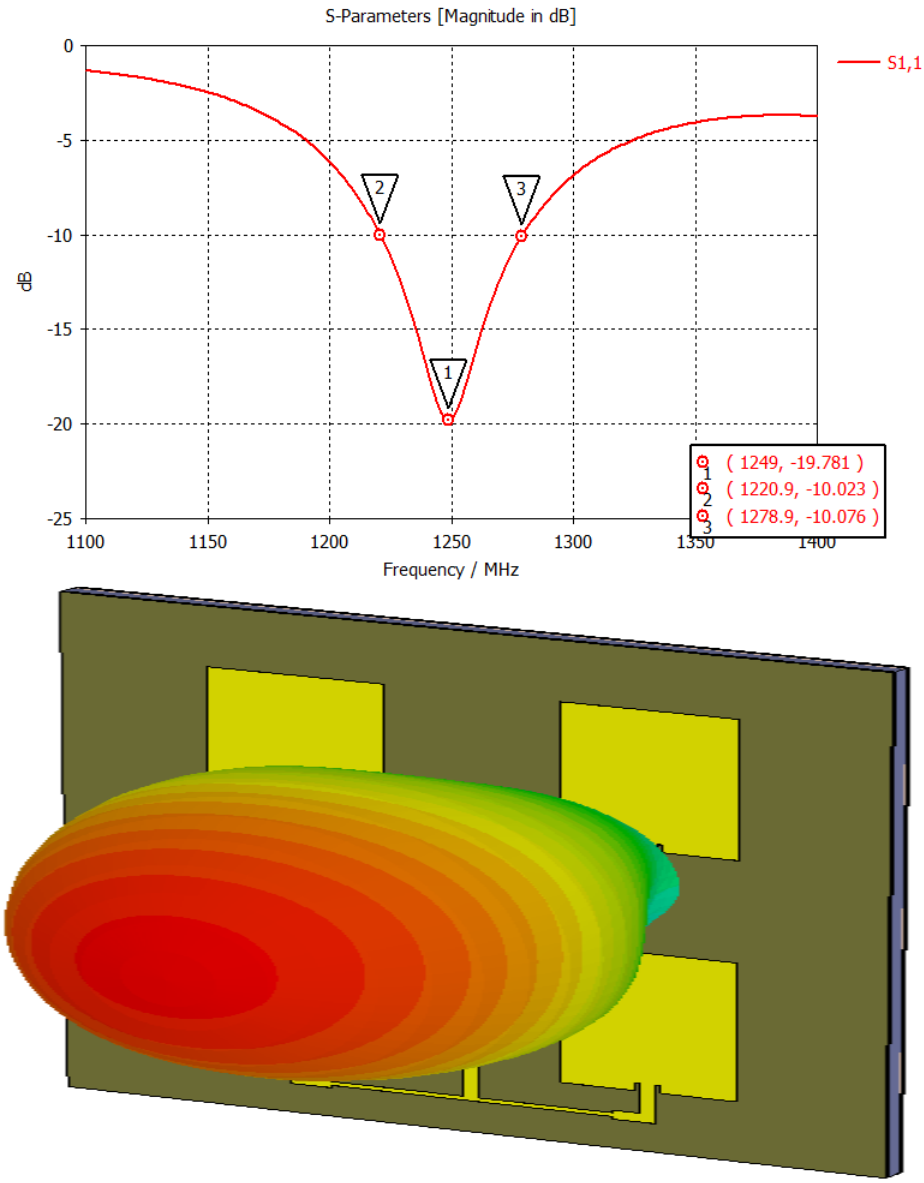

Figure 4.12

(a) Radar patch antenna S_{11} plot and (b) 3D beam pattern

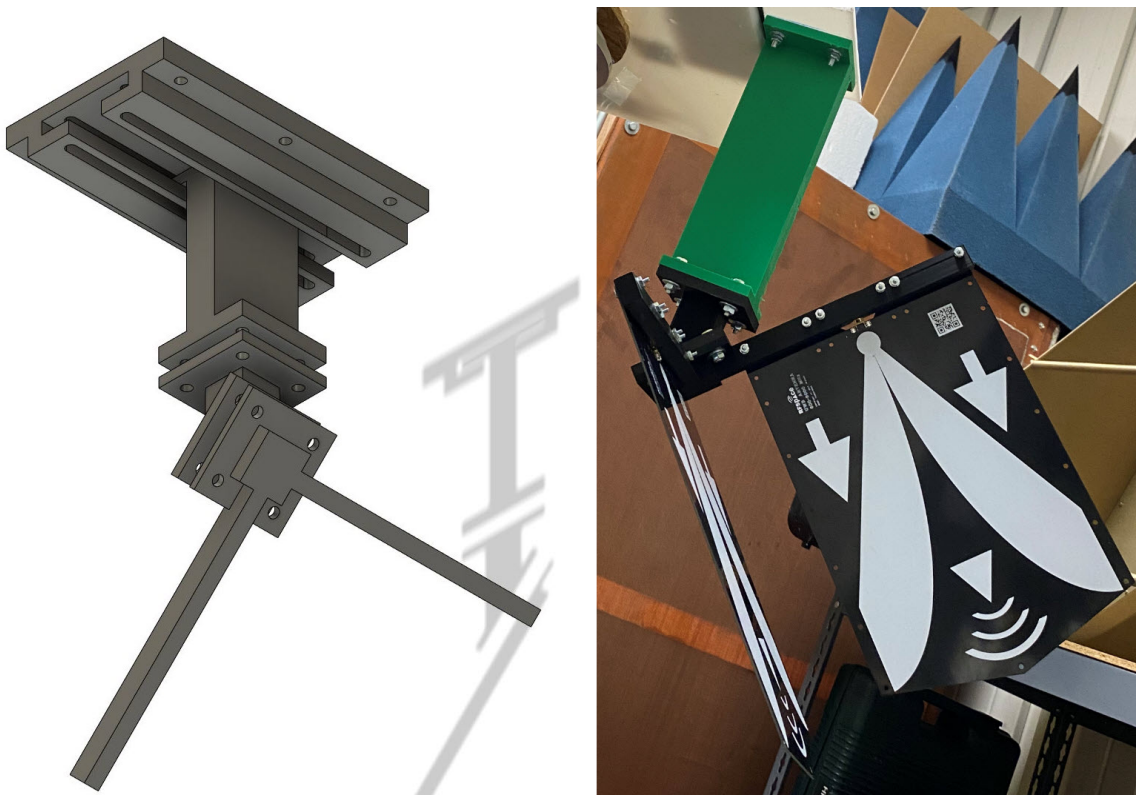

Figure 4.13

(a) Vivaldi antenna mount schematic and (b) printed design

angle of the targets was not disturbed when adjusting the orientation of the horn antennas and lowering and raising the mast. This approach of adjusting the antennas during testing for the UAS-based scatterometer is not feasible. This would require four different flights of the system while ensuring each flight path is geo-spatially identical and the antennas' orientation to the target is also identical during the four flights. This is difficult and it is not a viable solution.

The solution is to dedicate one antenna as a vertical antenna and to dedicate a second antenna as the horizontal antenna to create the four polarizations. This solution lends it self to being ideal for cross polarization measurements but not for co-polarization measurements. In order to create a viable co-polarization testing setup, a microwave circuit is needed to redirect the microwave energy between the antennas such that the antennas can create four polarizations.

The VNA currently transmits out of one port and receives in another port. In order to accommodate the capabilities of the VNA, the microwave circuit in the UAS-based scatterometer utilizes 4 RF coxial switches, a 20dB gain RF amplifier, and 2 directional couplers. The circuit is shown below Figure 4.14.

This circuit uses two coaxial RF switches to determine which polarization is selected for the device. One switch determines which antenna is connected to the transmit chain and the second switch determines which antenna is connected to the receive chain. Two additional switches are used to send the transmitted signal directly through a 20dB attenuator and back into the receiver. This is used as a means of internal calibration of the scatterometer. The transmit chain is connected to the coupling ports of the directional couplers. The antennas are connected to the input ports of the directional couplers. The receive chain is connected to the output ports of the directional couplers.

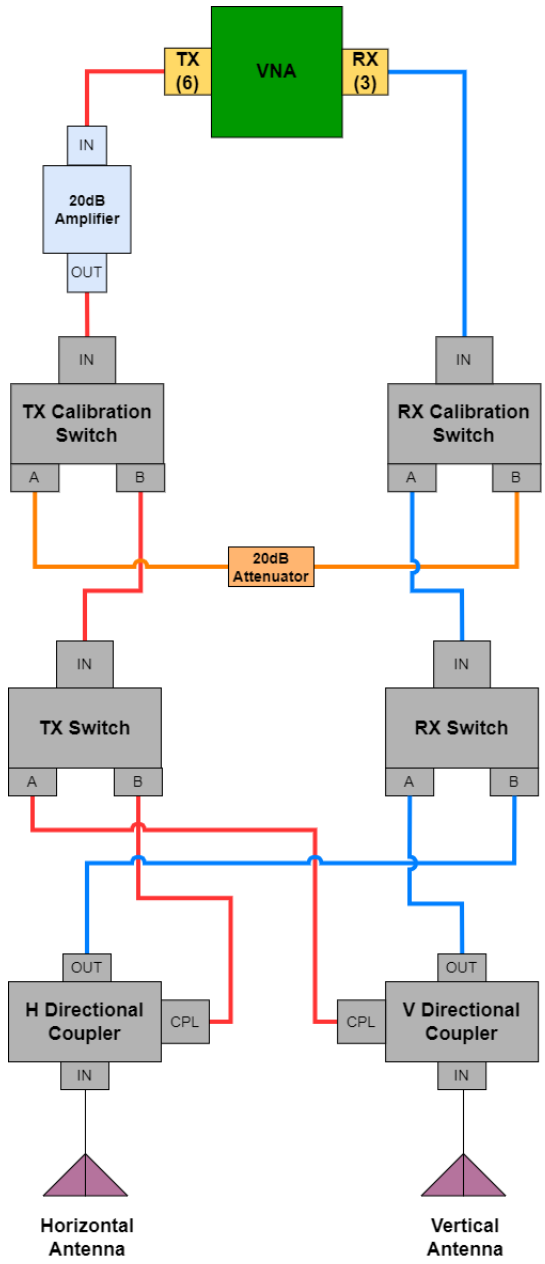

Figure 4.14

UAS-based scatterometer RF circuit

When using the same antenna for a co-polarization measurements, there is a need to ensure a moderate to high isolation of the transmit and receive chains. There is a 10dB coupling loss between the input port and the coupling port of the directional coupler. In order to mitigate this, a 20dB gain amplifier is added to the transmit chain. The directional couplers have a directivity of 36dB in the scatterometer's frequency range meaning the difference of forward power through the input port from the coupling port is 36dB higher than the forward power through the output port from the coupling port. The isolation between these two chains, specifically the isolation between the coupling port and the output port of the directional coupler is defined as the directivity and coupling loss added together. This results in a isolation of approximately 46dB.

The RF switches are controlled by 24V logic which can be achieved with an Arduino Mega 2560 and 8 5VDC relays. The logic circuit is shown in Figure 4.15. When either the A or B pin of the RF switch is sent to the GND of the 24V power source and the other pin is left open, the switch will allow the microwave energy through the grounded port. The Arduino can be used to excite the 5VDC relay to close the connection between the RF coaxial switch pins and the 24V battery's ground.

4.2.2 Integration and Operation

With the UAS-based scatterometer developed, the next step is to ensure the system is robust and easily controlled in testing. The UAS payload is equipped with an Intel Nuc computer which controls the VNA software and the Arduino switch control logic. In order to mitigate system intervention once the UAS has been deployed, a router is equipped to the payload and a remote desktop connection is created between the on-board computer and a computer on the ground that

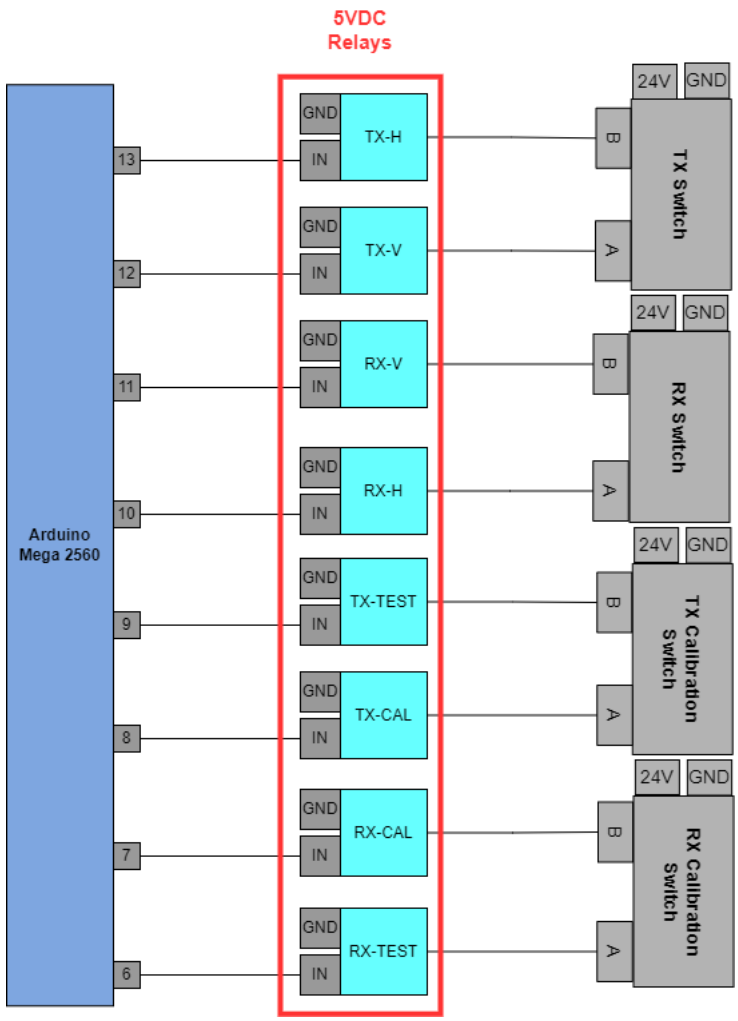

Figure 4.15

UAS-based scatterometer RF circuit control logic

is used by the researcher. The overall UAS-based scatterometer schematic is shown in Figure 4.17 with the RF switching circuits displayed a lumped device.

As the UAS-based scatterometer control software is derivative of the ground-based scatterometer and the GPR which also uses the VNA from the air, the Python-based GUI is adapted for the GPR's GUI, shown in Figure 4.18. This GUI allows the user to select which polarization is

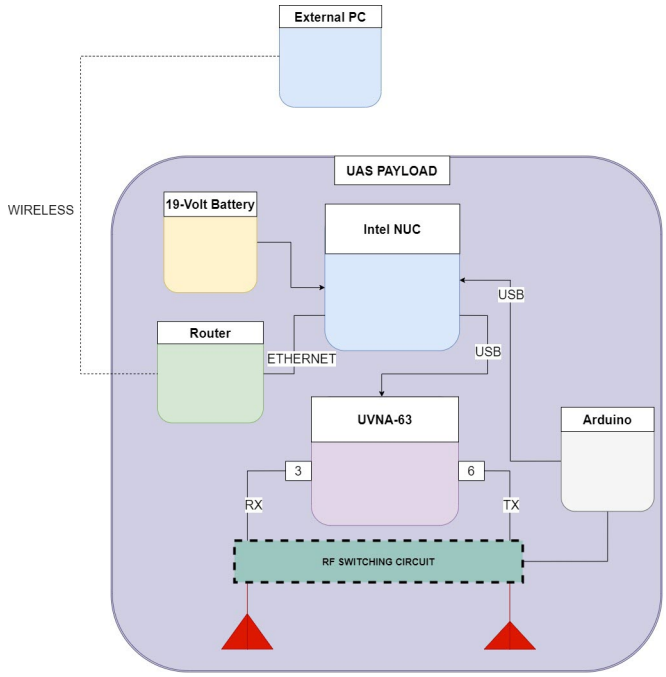

Figure 4.16

UAS-based scatterometer system schematic

used for testing while in the air. There is an "All" option in the GUI that will switch the path of the microwave energy for every scan of the scatteormeter rotating between the four polarization options. There is a "Calibration" option in the GUI that redirects the transmitted signal through a 20dB attenuator and sends it back to the receiver. This is used as a means of internal calibration for the VNA. The difference between the energy transmitted after being amplified by 20dB and then attenuated 20dB should result in 0dB. Any deviation in this across the operating band of the scatterometer can be documented and used to bias the returned tests data to further calibrate the response.

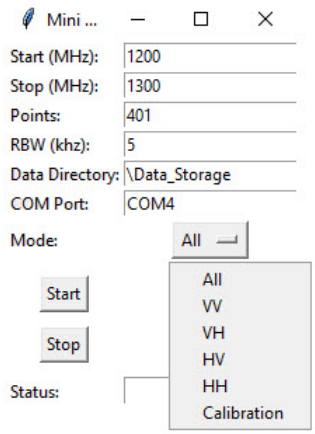

Figure 4.17

UAS-based scatterometer Python GUI

4.2.3 Calibration Procedures

In practice, the scatterometer will perform testing with the four polarizations (VV, VH, HV, HH) using a 1ft diameter circular plate and dihedral reflector made of two 1ft by 1ft squares. The targets are milled from 1/8-in aluminum and mounted to a 4ft stand made of PVC. The calibration testing follows the procedure shown in Table 4.1 to obtain the needed data in the most time efficient order.

The collected data is then brought to MATLAB for processing. The calibration scripts, shown below Figure 4.12, bring in the data that is stored in the "data" folder and isolate the collected S_{21} returns and maps it into a chirp Z-transform that fits a Kaiser window across the data and brings it into the time-domain. The preceding calibration algorithms are implemented and the background response is calculated and recorded as "Background" and calibration coefficients are stored as

Table 4.2

Testing procedures to collect calibration target data for circular plate and dihedral reflector

Calibration Order	(1) VV-Polarization	(2) VH-Polarization	(3) HH-Polarization	(4) HV-Polarization
1st	Ground	Dihedral Horizontal	Ground	Dihedral Horizontal
2nd	PVC Stand	Dihedral 45° Counter-Clockwise	PVC Stand	Dihedral 45° Counter-Clockwise
3rd	Circular Plate	Dihedral 45° Clockwise	Circular Plate	Dihedral 45° Clockwise
4th	Dihedral Vertical	Dihedral Vertical	Dihedral Vertical	Dihedral Vertical
5th	Dihedral 45° Clockwise	Circular Plate	Dihedral 45° Clockwise	Circular Plate
6th	Dihedral 45° Counter-Clockwise	PVC Stand	Dihedral 45° Counter-Clockwise	PVC Stand
7th	Dihedral Horizontal	Ground	Dihedral Horizontal	Ground

"avgRawDataCAL". This value is used in subsequent testing to characterize the target and ensure meaningful data from the system.

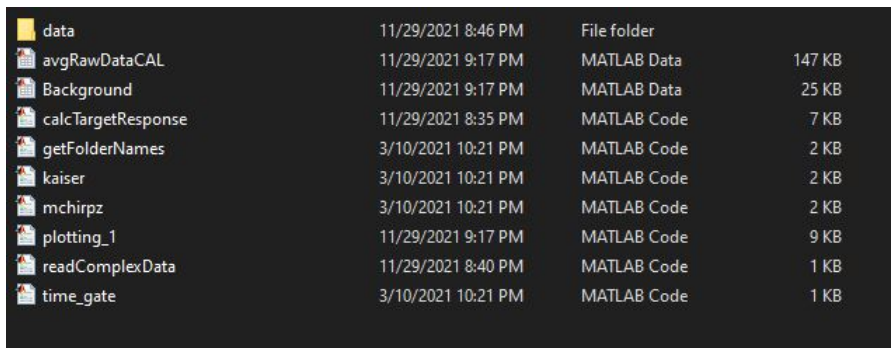

Figure 4.18

Scatterometer post-processing code

CHAPTER V

RESULTS

This chapter serves to present the results of both the GPR and scatterometer systems as well as their efficacy.

5.1 Power Amplification

The scatterometer is designed to gather energy that is reflected back from a distributed target. Typically, the energy reflected back to the scatterometer is significantly less than the energy propagated initially from the scatterometer. In order to have a substantial received power that exists well above the noise floor, a few things can be done. The most direct solution is to increase the incident energy on the target by having a higher output power from the transmitter. This is achieved by adding an RF amplifier stage in the transmit chain of the VNA before sending the signal into the horn antenna, illustrated in Figure 5.1.

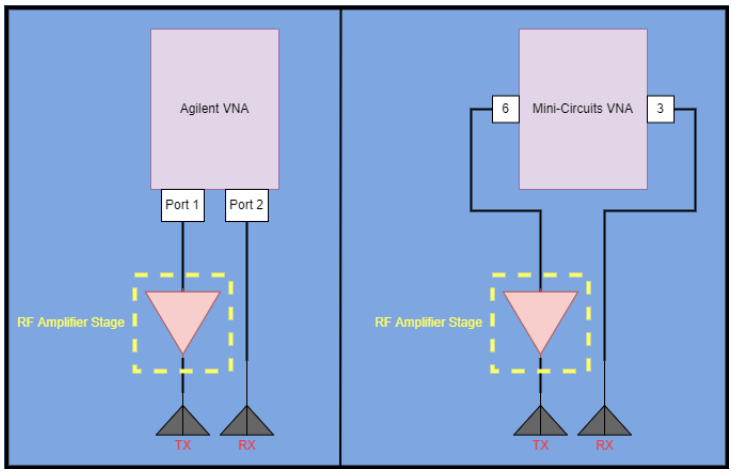

Figure 5.1

Initial ground-based scatterometer test setup for (a) Keysight FieldFox and (b) UVNA-63

The current maximum output power for both VNAs is 0dBm or 1mW. In order to mitigate part of the loss through propagation over the distance from the top of the mast to the target and back, the signal power needs to be increased. Shown below in Figure 5.2 is the first amplifier that was tested for increasing the signal power. This RFLambda RAMP00G18GA is a DC-18GHz RF amplifier with a typical gain of 31dB and a typical 1db compression (P1dB) of 26dbm [9]. This means that with an output power of -6dBm from the VNAs, the signal strength should be increased to 26dBm.

An experiment was conducted with the scatterometer to determine the efficacy of the amplifier. Using the standard testing parameters, all of the calibration targets were imaged twice, once without the amplifiers connected, and once with them connected. Below, the responses for both tests are shown for the circular plate co-polarization returns in Figure 5.3.

This test revealed significant problems. Looking at the target responses, it appears that the power level for both direct coupling between the antennas and the target are approximately 20dB higher for the non amplified response that the amplified response. As this is potentially a substantial

Figure 5.2

RFLambda RAMP00G18GA amplifier

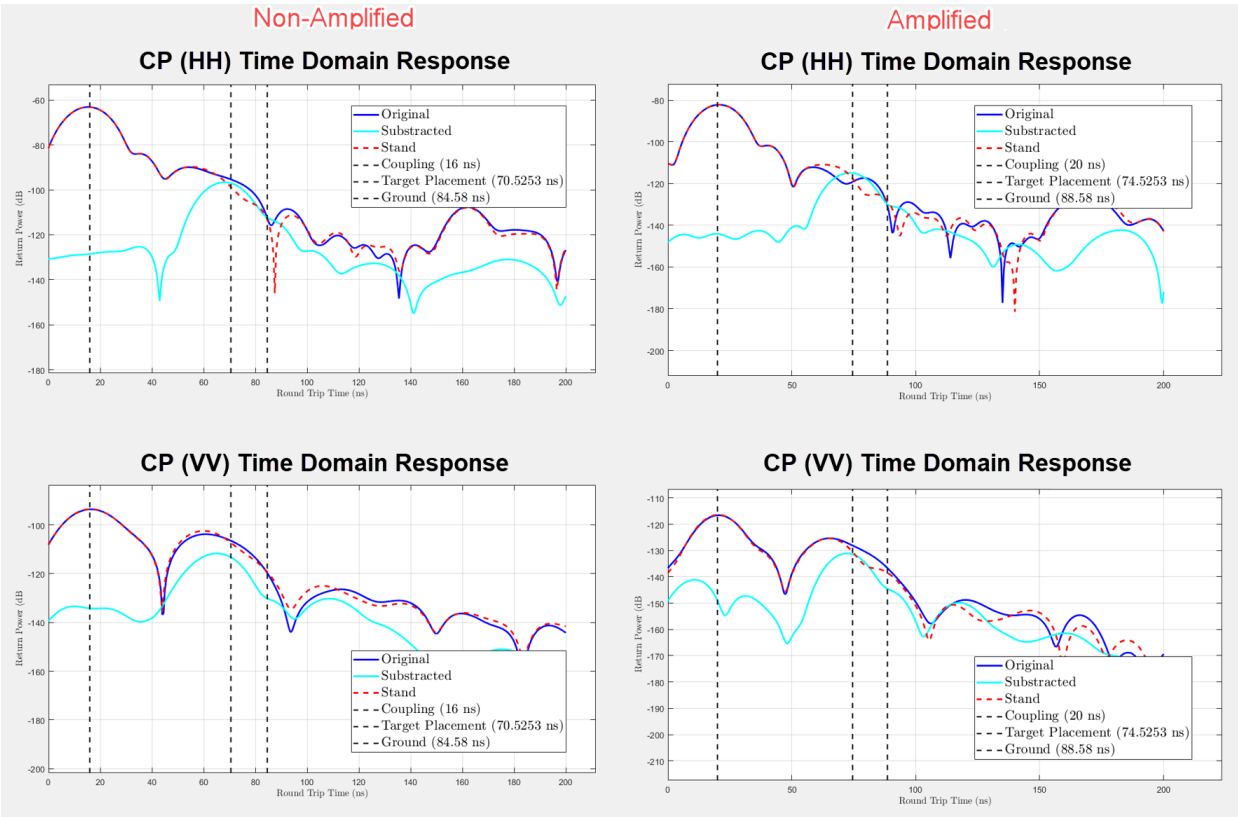

Figure 5.3

Field test of circular plate with (a) HH polarization with no amplifier (b) HH polarization with amplifier (c) VV polarization with no amplifier (d) VV polarization with amplifier

issue moving issue forward, the amplifier needed to undergo further testing to determine if it is operating incorrectly or there was simply problems in the testing procedures during the experiment. The Agilent Microwave Analyzer's spectrum analyzer and vector network analyzer functions are capable of testing the amplifier to determine if there are any issues. The testing setup is shown below in Figure 5.4.

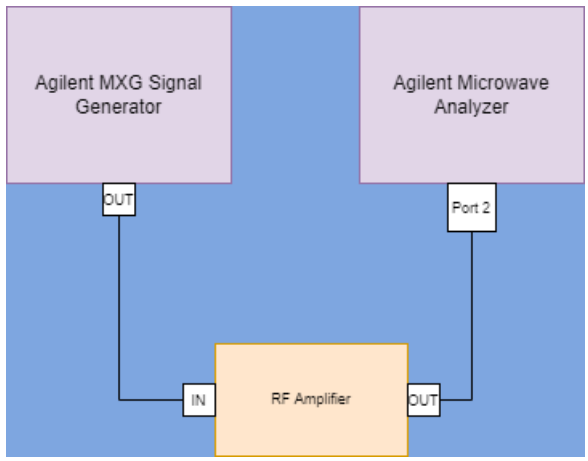

Figure 5.4

RFLambda amplifier troubleshooting setup

An Agilent MXG analog signal generator is used to create a sine wave at 1.5GHz. As a baseline to ensure the signal generator is operating correctly, a -20dBm signal is sent from the signal generator into the spectrum analyzer for analysis and the result is shown below in Figure 5.5.

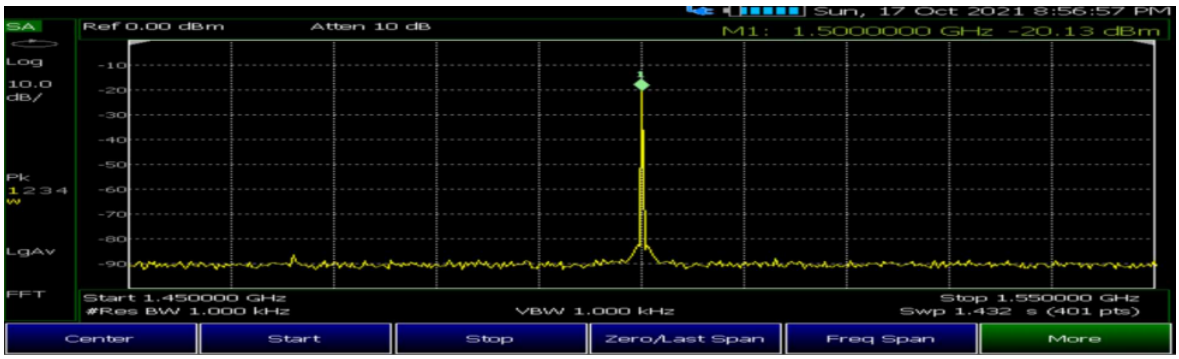

Figure 5.5

Signal generator at -20dBm

The spectrum analyzer shows a clean response at 1.5GHz with a power level of -20dBm. With this the amplifier can be tested. The signal generator is connected to the amplifier and its output to the spectrum analyzer. The typical gain of the amplifier is 31dB, so the expected power level at the spectrum should be 11dBm, which is within the bounds of the microwave analyzer which can receive signals of up to 27dBm. The response is shown below in Figure 5.6.

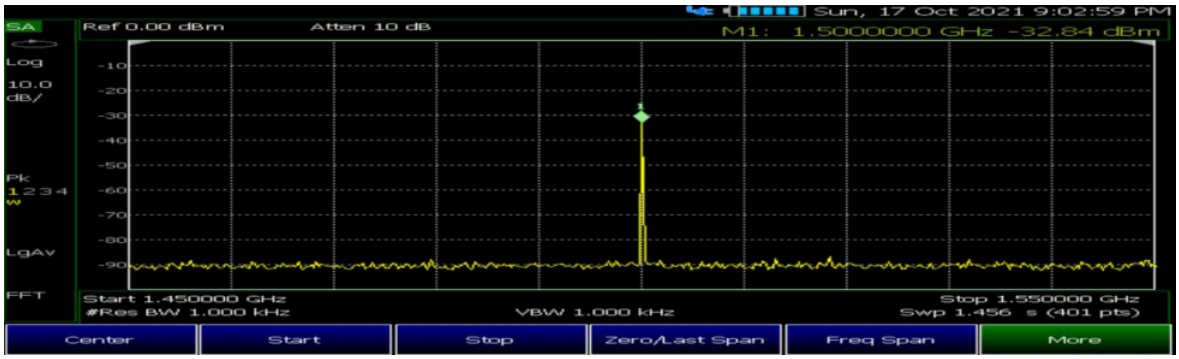

Figure 5.6

RFLambda amplifier test 1

This response shows the returned signal at -32.8dBm. This means the amplifier is attenuating the signal by 10dB. With this information, a second test is performed where the signal generator is set to -10dBm output and the response through the amplifier is observed below in Figure 5.7.

This test shows the response at the spectrum analyzer is -20dBm which is a 10dB attenuation from the input signal to the amplifier. From this test there is further verification there is something wrong with the amplifier. A final test is ran using the VNA of the microwave analyzer. Port 1 of the VNA is connected to the RF amplifier and the output is sent to Port 2 of the VNA. The S_{21} response is shown between 1-10GHz at an input level of -15dBm. This test shows the difference in power between the two ports. If the amplifier is operating correctly, the expected response should be a line across 30dB meaning the power at Port 2 is 30dB higher than the power sent from Port 1. The response is shown below in Figure 5.8.

This test shows that across the bandwidth, the amplifier is degrading the signal by an average of 10dB contrary to increasing it by 30dB, with the exception of the band between 1.5-2GHz which is degrading the signal by roughly 14dB.From these experiments, it is concluded the amplifier is

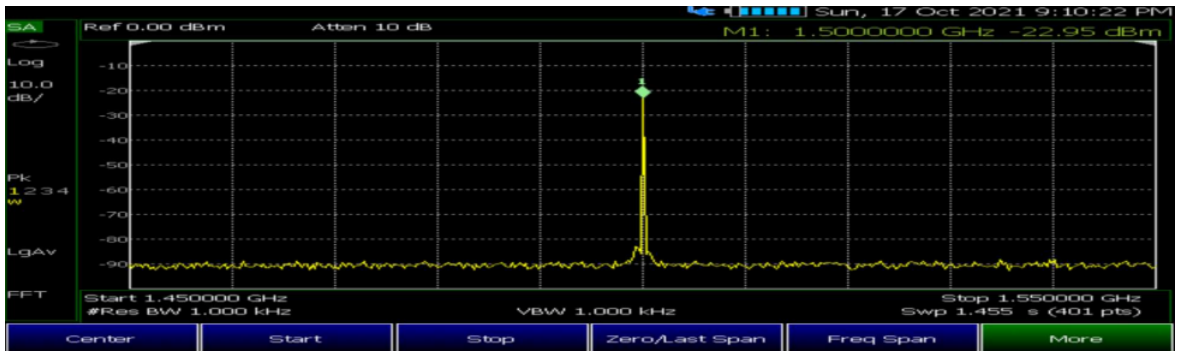

Figure 5.7

RFLambda amplifier test 2

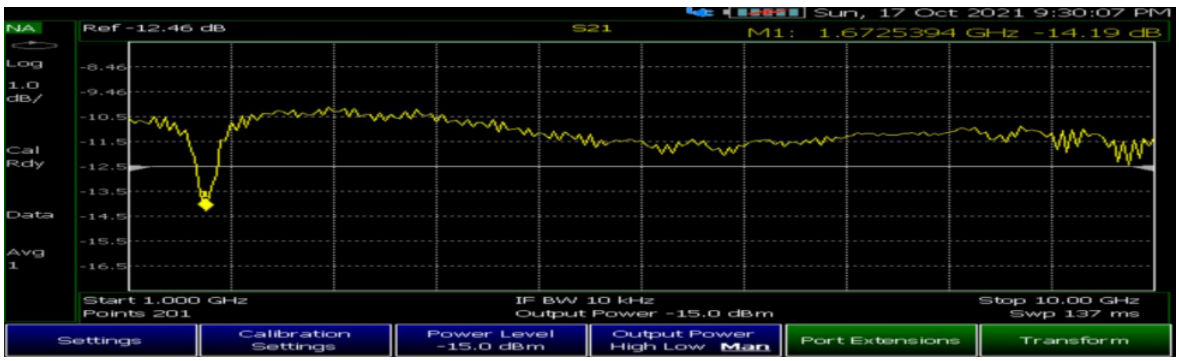

Figure 5.8

RFLambda amplifier response across the band

corrupt and needs to be replaced. The search for a new amplifier began and ones were recommended to replace the previous amplifier. There were, however, amplifiers available in the lab that were considered for replacement. Two ZX60-H242+ RF amplifiers, shown below in Figure 5.9, were found to be viable for the experiment. While there bandwidth is not as wide as the inoperable amplifier bandwidth, it does exist within the standard parameters of the scatterometer (700-2400MHz).

Figure 5.9

ZX60-H242+ RF amplifier

The amplifiers have a standard gain of 14dB in the scatterometer's bandwidth, a P1dB of approximately 22.8dBm, and maximum RF power input ratings of 24dBm [6]. The solution for our system is to cascade them together so achieve an output power above 20dBm. A test was created to test the amplifiers using the Agilent microwave analyzer. The VNA is used to send a 0dBm signal from port 1 into the cascaded amplifiers. In order to ensure safety of the analyzer, a 30dB attenuator is placed on the output of the amplifiers before sending the signal into the VNA. The response is shown below in Figure 5.10.

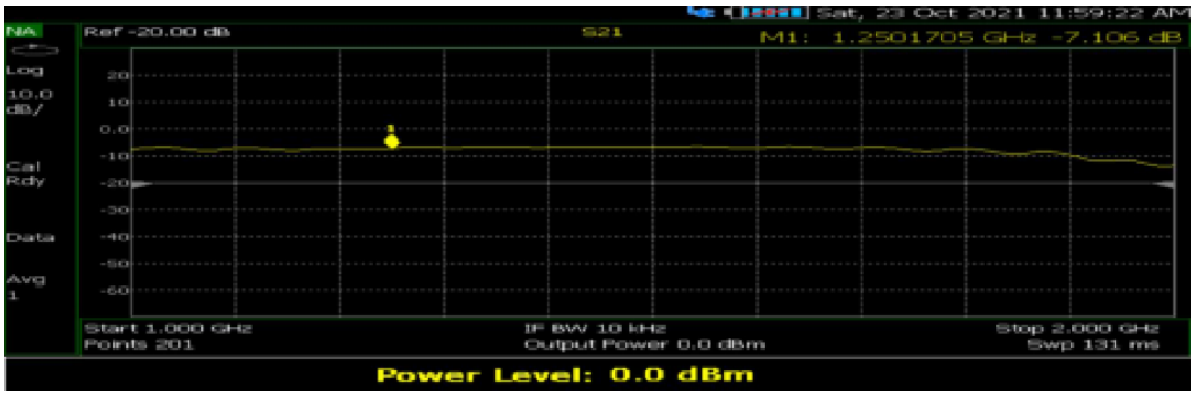

Figure 5.10

ZX60-H242+ cascade test

This show the average power difference between the two ports is -7dBm. Accounting for the 30dB attenuator, the resulting power amplification is approximately 23dBm. This is acceptable for our testing setup and is added to the transmit line of the scatterometer.

In order to improve both the maximum power output of the transmitted signal as well decrease the need for cascaded amplifiers which can cause issues in the overall fidelity of the scatterometer, a new amplifier was purchased for use in the final design of the scatterometer. The Pasternack PE15A3008 RF amplifier, shown in Figure 5.11, has a standard gain of 27dB with a P1dB of 25dBm [7]. This unit operates with a 12 volt feed power which is already available on the platform and allows for approximately 30 milliwatts of transmit power.

Figure 5.11

PE15A3008 amplifier

The results of the new amplifier are shown in figure 5.12 where the S_{21} response of the amplifier sits around 27dB over the operating bandwidth.

5.2 GPR Results

Once the GPR payload was created, there was a need to characterize its performance. First the GPR is tested in an anechoic chamber. Once the GPR is placed in the anechoic chamber, it is initiated, shown in Figure 5.13 and allowed to run for 5 minutes. After approximately 5 minutes, the data is saved, transformed to the time-domain, and stored and the response is shown in Figure 5.13. There is a consistent return at 5 nanoseconds. This is due to the direct coupling between the

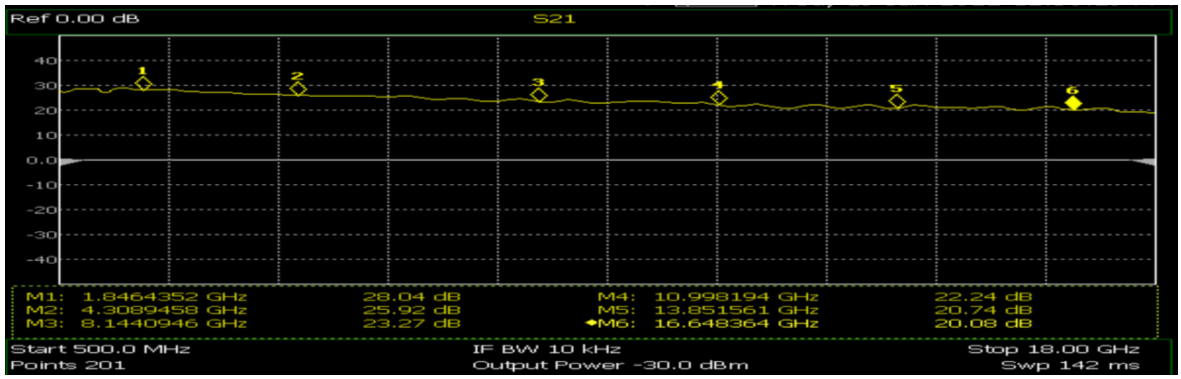

Figure 5.12

PE15A3008 amplifier S_{21} response

antennas as the receiving antenna is within the reactive near field of the transmit antenna together with the phase delays from the coaxial cables. This response is saved and can be removed in future tests of the GPR.

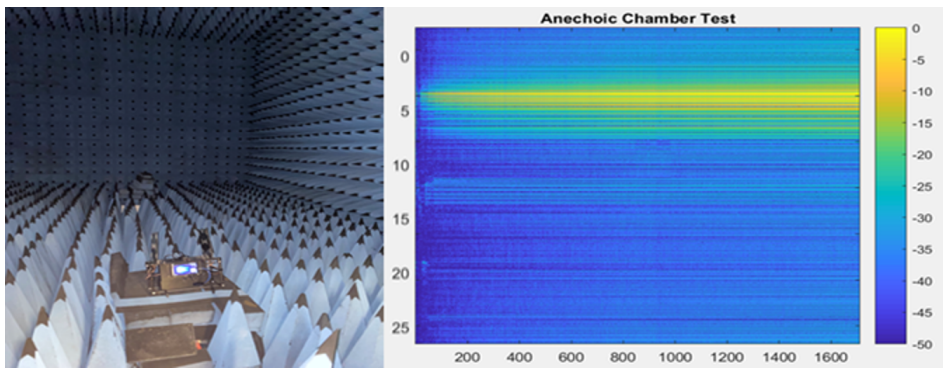

Figure 5.13

(a) GPR in anechoic chamber and (b) b-scan response

After the inital GPR measurements,more tests are done in the lab for further characterization of the GPR unit. The GPR was placed on a rolling cart and rolled past a wall where a 1 square-foot

aluminum plate was placed approximately 8 inches away from the wall, shown in Figure 5.14. The response, shown below, yields a hyperbolic response that matches the expected GPR target return.

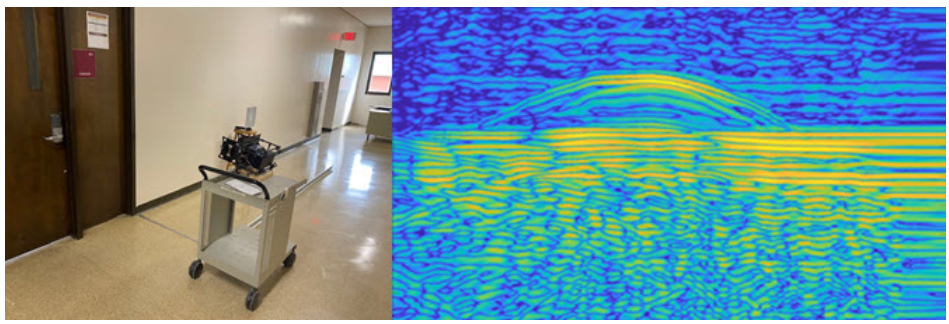

Figure 5.14

(a) GPR on rolling cart scanning a metal plate and (b) B-scan response

With the GPR performance characterized, it was ready for field testing. The payload was attached to the UAS and is shown in Figure 5.15.

Figure 5.15

(a) GPR payload and (b) GPR performing data collection

In order to test the efficacy of the unit, the GPR was brought to a field site for experimentation, illustrated in Figure 5.16. The field has a variety of targets buried at approximately known location. The procedure for testing is to initiate the GPR and then to ascend the UAS to flight altitude. Once at flight altitude, the GPR can begin its test path. The GPR flew in 6 lines across the field of roughly 100 meters in length, spaced roughly 3 meters apart. With a scan frequency of 33Hz and a flight speed of 5 m/s, this results in one scan for every 15cm of linear travel.

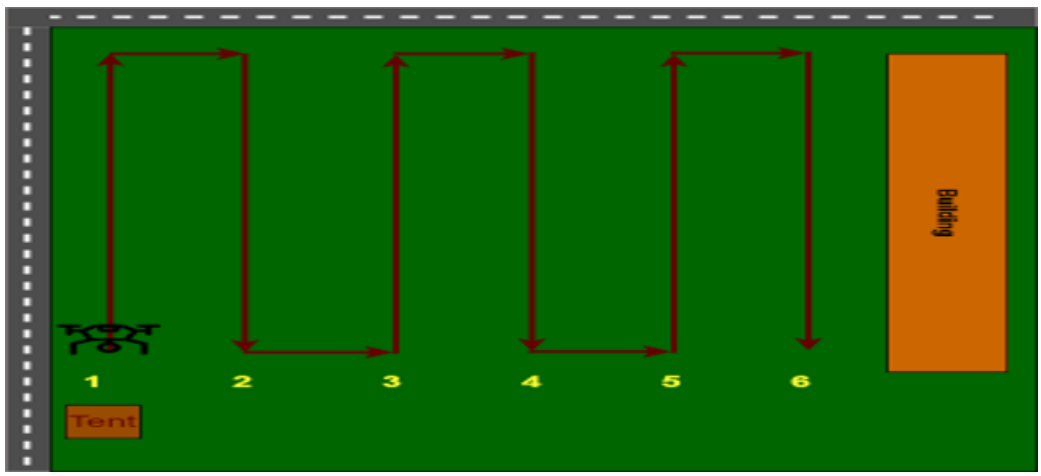

Figure 5.16

GPR testing field layout and flight path

After field testing, the return data was saved and processed in MATLAB. To create a high resolution response in the data for object detection, the frequency domain data was multiplied with a frequency domain representation of a differentiated Gaussian pulse, shown in Figure 5.17. This is a method of raising the resolution of A-scans and B-scans. This resulting data was then changed from the frequency-domain data to the time-domain.

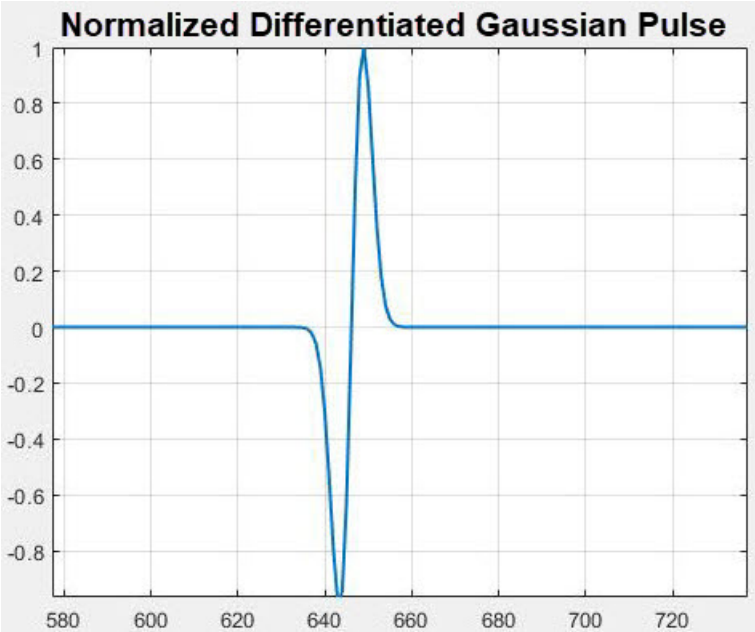

Figure 5.17

Differentiated Gaussian pulse time domain response

The B-scan of the data is shown in Figure 5.18. There are a few attributes in the data that need to be resolved to clearly observe objects in the ground. The first attribute to consider are the intital and ending A-scans in the data. They appear blurry and do not look to have meaningful characteristics for the object detection. After analyzing the process of testing, it was found that they are just consequence of the steps to test the GPR. The GPR is started and stopped while the UAS is on the ground. This creates large reflections that are due to the coupled responses between the two antennas as well as the ground return as the ground surface is within the reactive near-field of the antennas. This information can simply be removed by gating the data in time to remove beginnings and ends of the data. The next attribute to consider is the high return from the ground surface which can be seen near the top of the B-scan. This is expected in the data and is simply the

direct coupling response from the two antennas. Using the data recorded in the anechoic chamber, this coupling can be calibrated out.

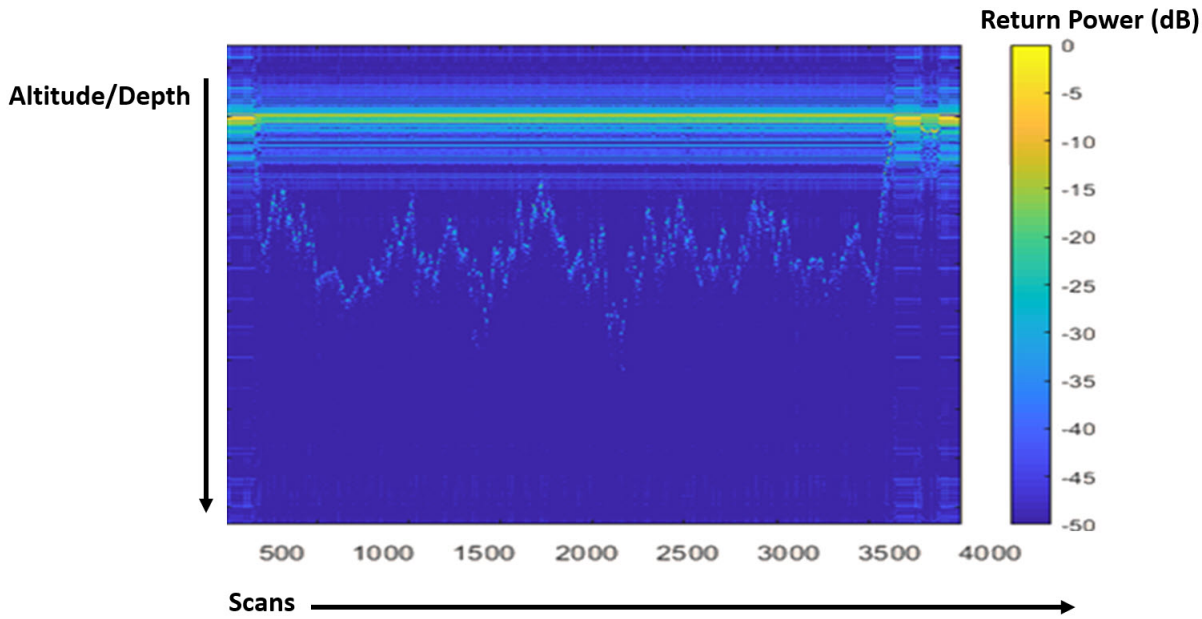

Figure 5.18

Initial GPR field test B-scan

After removing these attributes, the ground reflections are more clearly visible. Ideally, the ground response would be consistent and appear as a horizontal line across the B-scan. In this data, the ground reflections are noisy and sporadic. This makes sense as on the day of testing, the UAS had significant issues maintaining altitude stability. Additionally, the ground is not level and flat across the field, adding to the noisy ground reflections. In order to detect the targets effectively, the ground returns need to idealized. This is achievable by mapping the ground reflections for all of the scans and then removing all of the data column-wise before the ground reflections peak values. This levels out the ground field and is show in Figure 5.19.

Once the ground height is normalized, subsurface target reflections can more clearly be seen on the B-scan image. However, the B-scan is a result of all scan lines from the field test. The scan lines need to be isolated in order to adequately discern targets in the field. By segmenting the B-scan, shown in Figure 5.20, targets begin to appear.

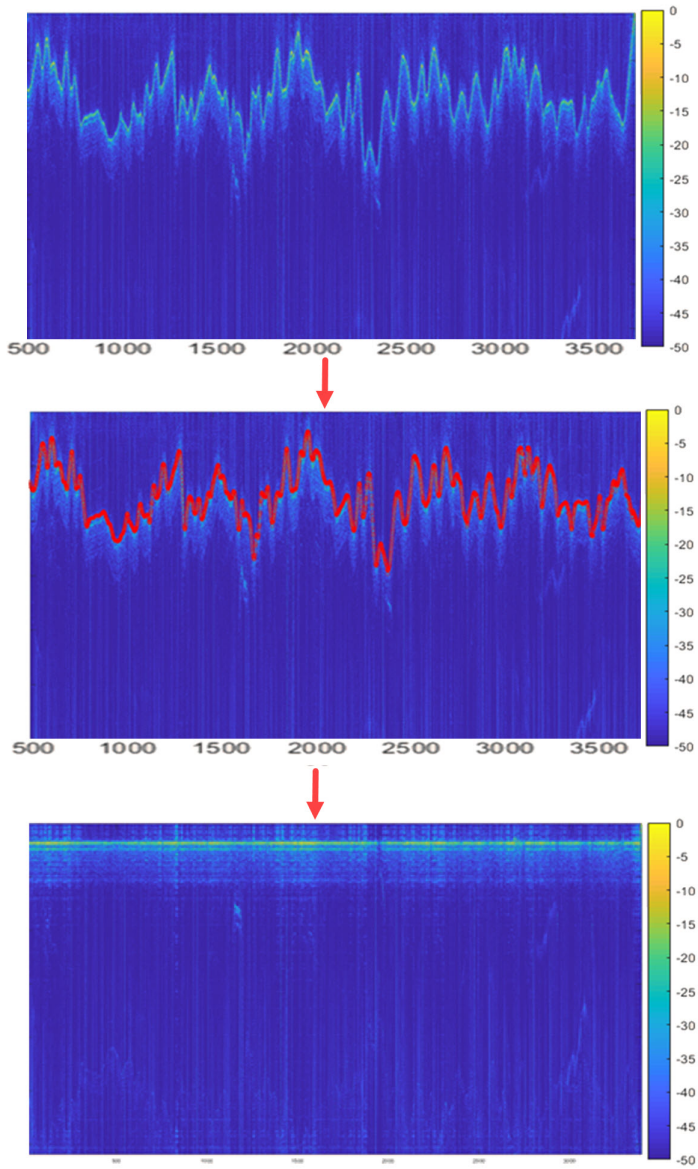

Figure 5.19

(a) B-scan denoised and (b) b-scan ground height mapped and (c) b-scan ground height normalized

In order to test the capabilities of the lidar unit, a test was conducted in the field with the lidar unit attached to the drone. The drone started on the ground and then oscillated up and down in altitude four times. The intent was that in time, the altitude-range data would appear as a sinusoidal

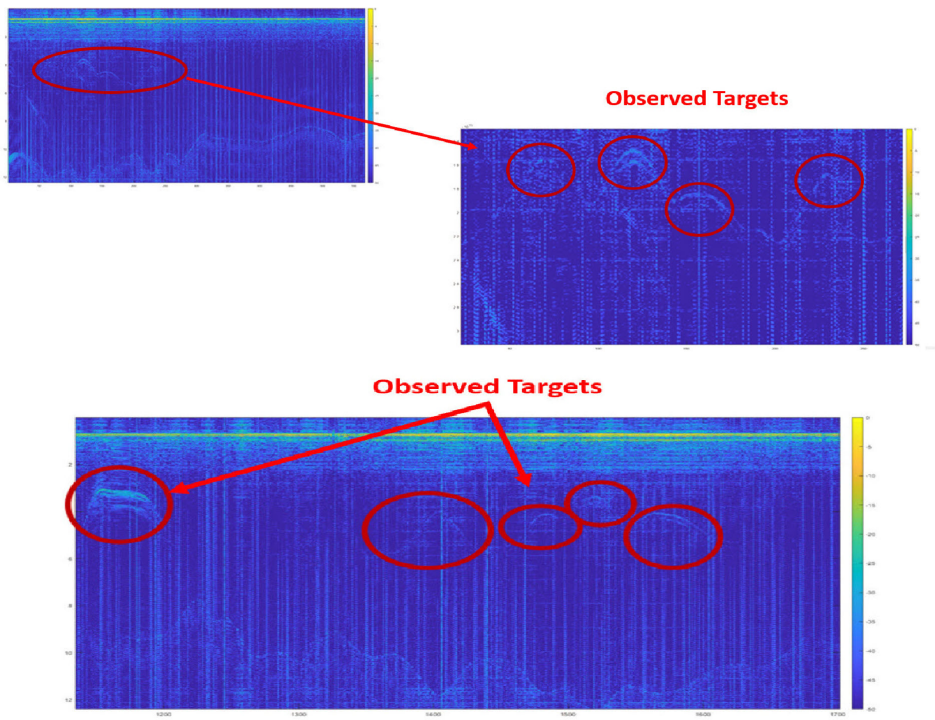

Figure 5.20

(a) B-scan targets From beginning of flight path and (b) B-scan from later in the flight path

signal when plotted. This concept is illustrated in Figure 5.21. After looking at the data, also in Figure 5.21, the sinusoidal response could be found but it appeared very rough and the signal was not a smooth sinusoidal response. The drone was until very recently, February 2022, not functioning well and had significant flight issues during this test. These flight issues seems to account for the non-ideal response in the lidar data, but the lidar range data collection needs to be tested further.

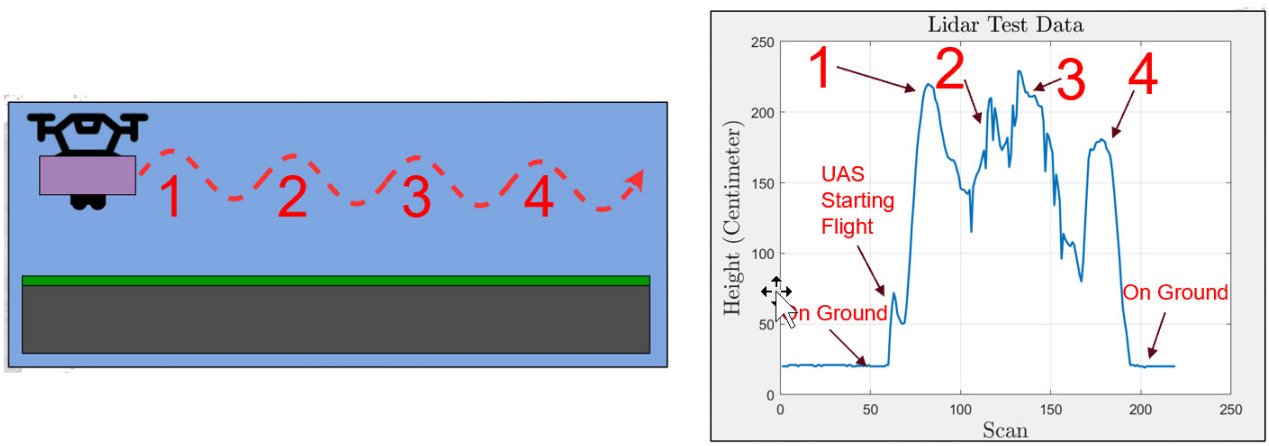

Figure 5.21

(a) Lidar unit field test and (b) range data from test

5.3 Scatterometer

This section outlines the results from both the ground-based scatterometer and the UAS-based scatterometer.

5.3.1 Ground-Based

The completed ground-based scatterometer is shown in Figure 5.22.

Figure 5.22

Ground based scatterometer imaging a dihedral reflector

In order to characterize the ground-based system, calibration target testing was performed. For the calibration targets, a circular plate and a dihedral reflector were used. The dihedral reflector has four orientations that can be imaged. The first step in calibration is to image the ground and PVC stand that holds the calibration targets. This results in 7 different target images for 4 different polarizations, totaling 28 different scans of the scatterometer. The testing setup is shown in Figure 5.23.

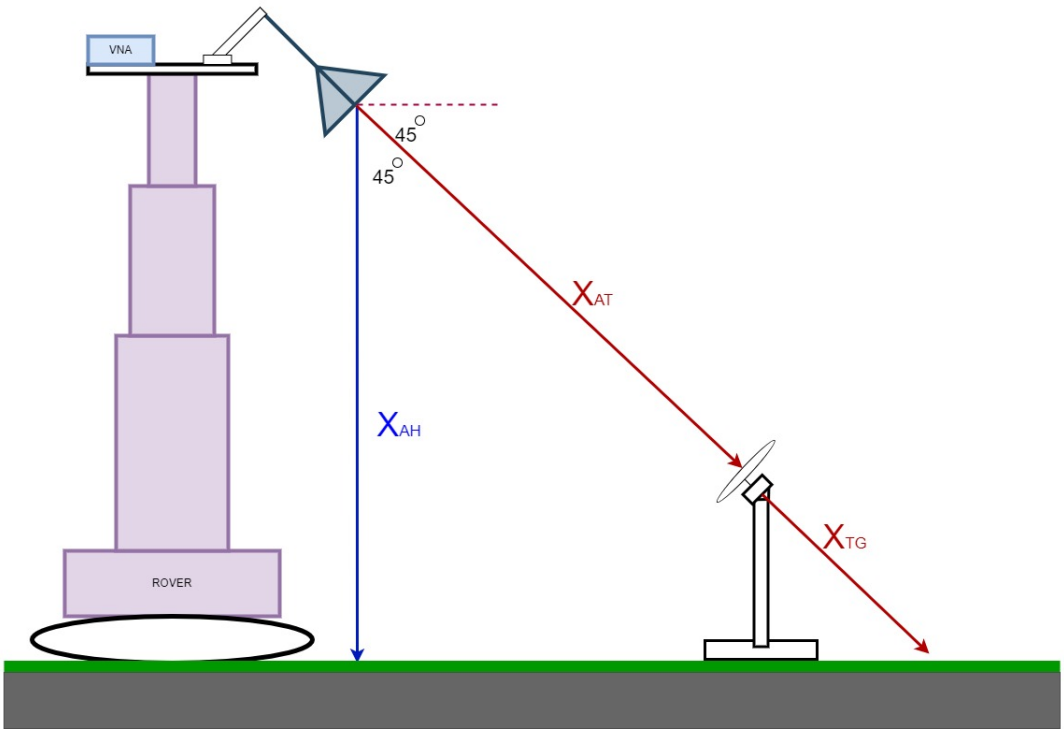

Figure 5.23

Ground-based scatterometer geometric test setup

The antennas are at a height, X_{AH} , of 22.3ft, validated by a laser range finder. With the antennas positioned at an angle of 45 degrees, a triangle is made from the antennas, the ground,

and the center of the antenna's beam pattern when it hits the ground. Given a 45-45-90 triangle and Pythagoras' Theorem, the distance from the antenna to the point where the beam hits the ground, $X_{AT} + X_{TG}$, is 31.5ft. Accounting for the height of the target, X_{TG} , the beam hits the target 5ft before it hits the ground, validated with a laser range finder. This puts the target at a distance of 26.5ft from the antenna. The round-trip time of the incident energy propagating to the target and the reflected echo propagating back to the scatterometer is 53 nanoseconds. The measured coupling between the two antennas is approximately 19 nanoseconds round-trip from the transmit port of the VNA to the end of the antenna. This means the reflections for the calibration targets should appear at the combined round trip time of 72 nanoseconds.

As a basis, the reflections for the PVC target and stand and the ground reflections are shown in Figure 5.24. These responses can be removed from the calibration target reflection to better isolate the calibration target responses.

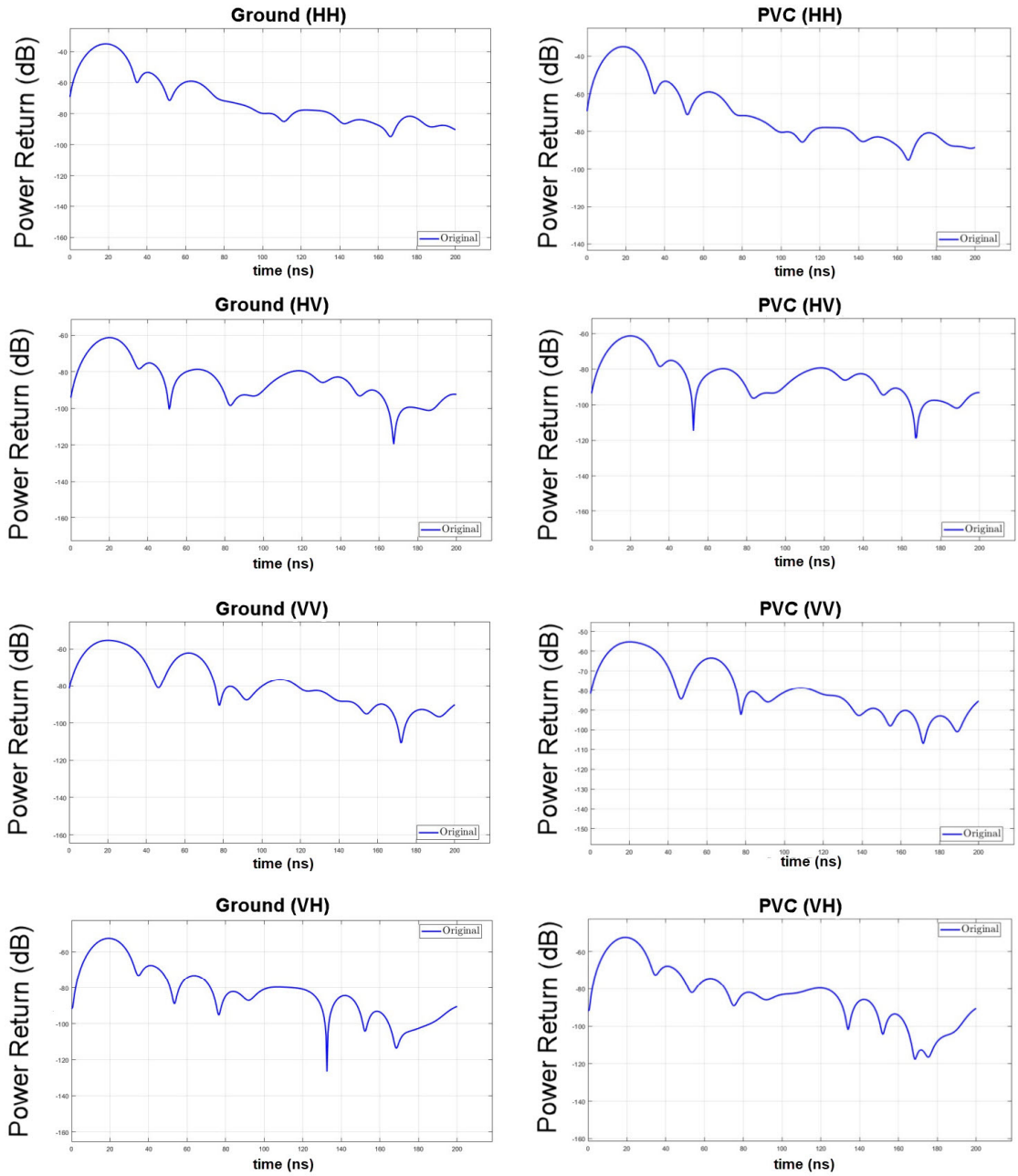

Figure 5.24

Ground and PVC Stand Response

The first calibration target responses is the circular plate shown in Figure 5.25. After subtraction of the PVC and ground response, there is a clear return at 72 nanoseconds for the co-polarization

configurations. There is little reflection for the cross polarization responses which is expected for the circular plate.

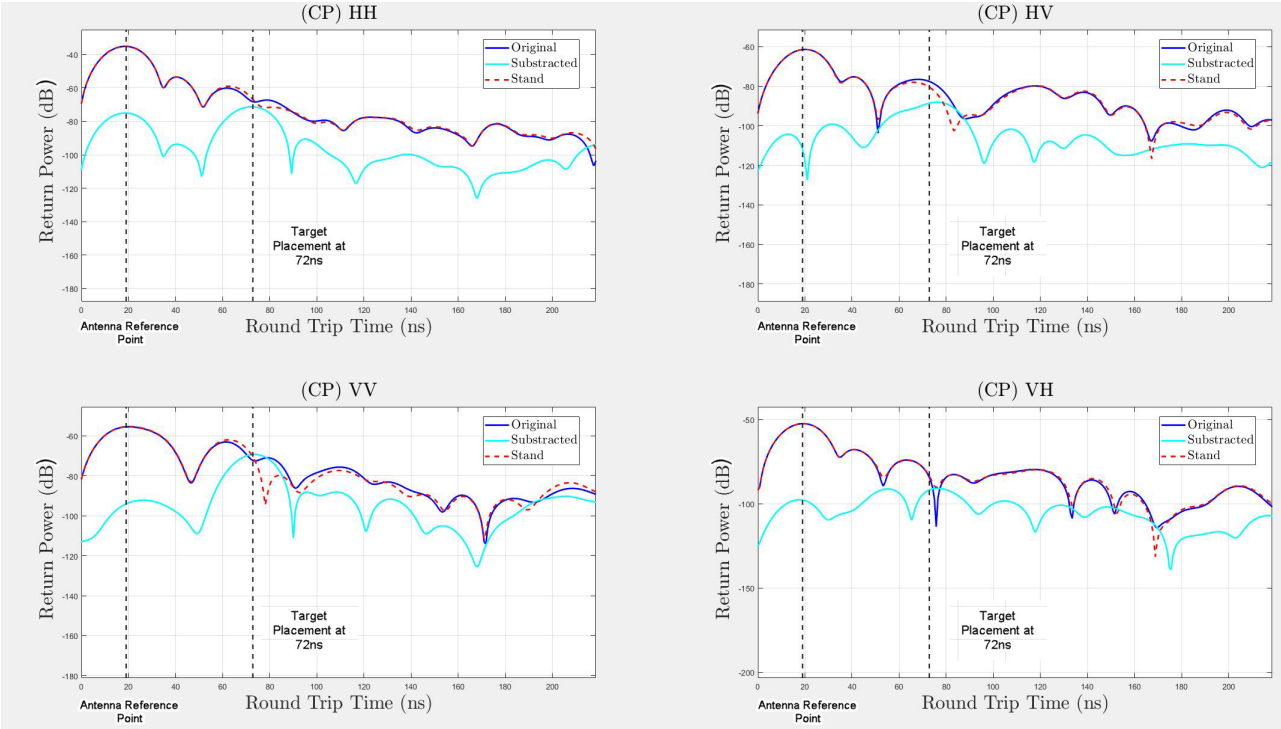

Figure 5.25

Circular Plate Response

The next target is the dihedral reflector. To characterize all four polarizations, the reflector is oriented in four different configurations (Vertical, Horizontal, Clockwise, Counter-Clockwise). The responses are shown in Figure 5.26.

There is a clear response after background subtraction at 72 nanoseconds for the co-polarizations which is expected for the vertical orientation.

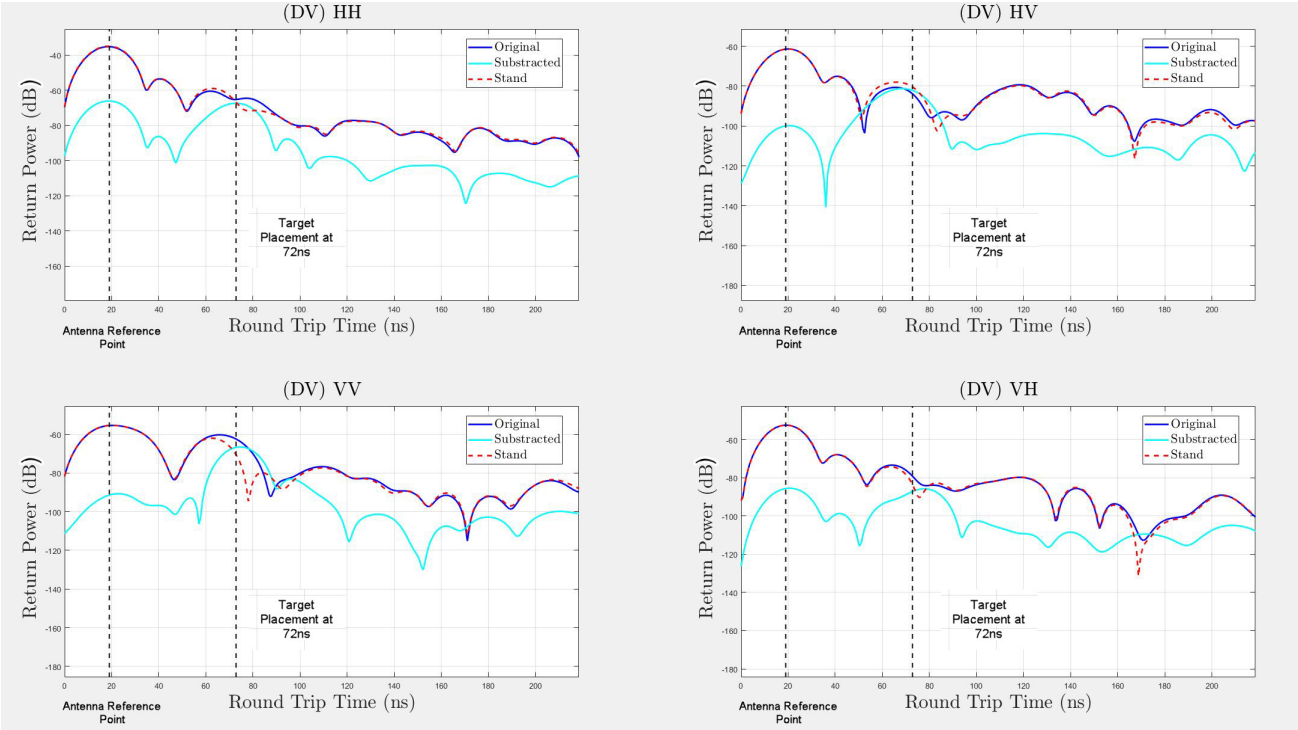

Figure 5.26

Dihedral Vertical Response

Similar to the vertical dihedral, there is a clear response after background subtraction at 72 nanoseconds for the co-polarizations which is expected for the horizontal orientation.

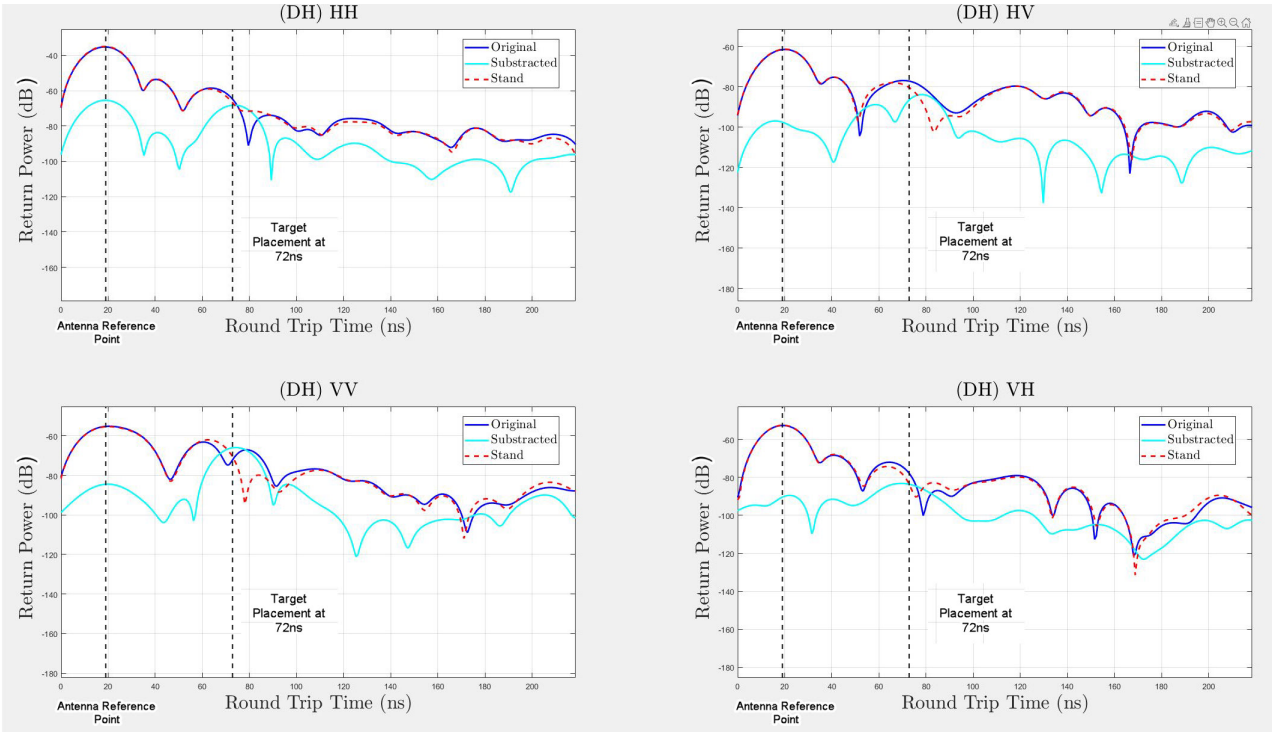

Figure 5.27

Dihedral Horizontal Response

There is a clear response after background subtraction at 72 nanoseconds for the cross-polarizations which is expected for the clockwise orientation.

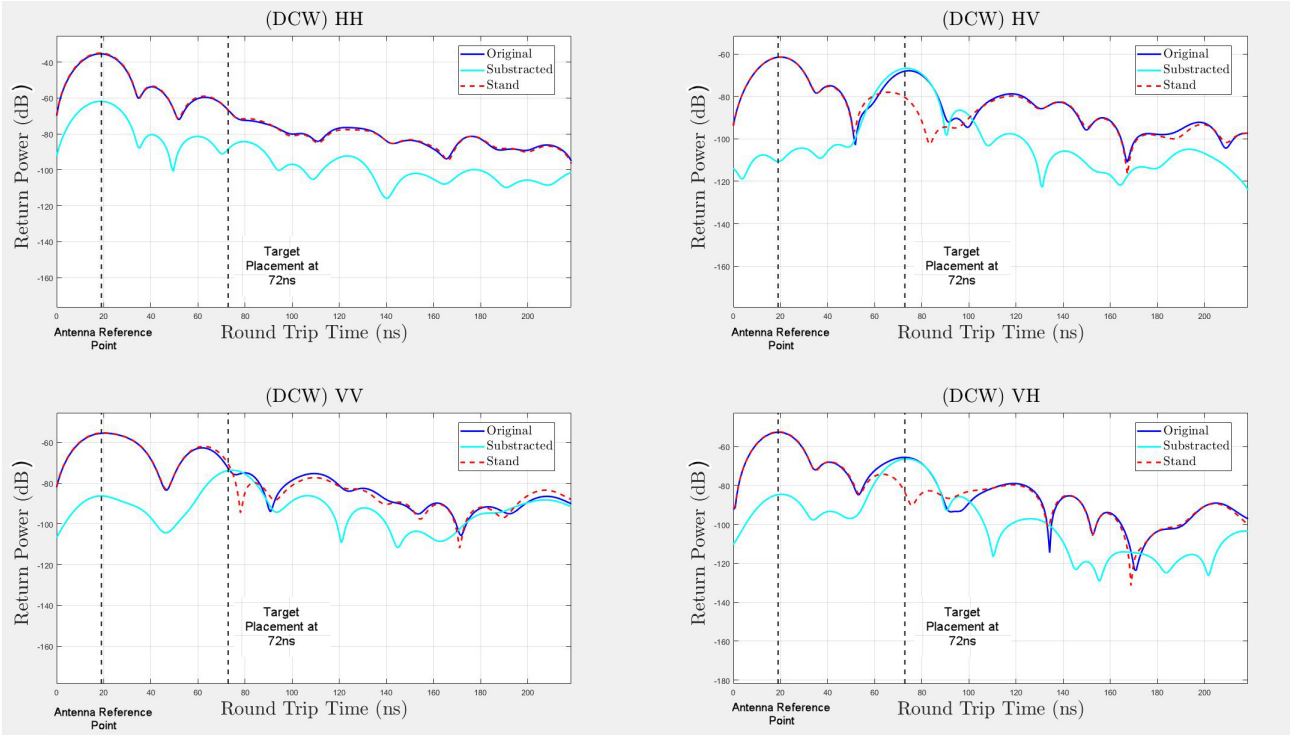

Figure 5.28

Dihedral Clockwise Response

Similar to the clockwise dihedral, there is a clear response after background subtraction at 72 nanoseconds for the co-polarizations which is expected for the counter-clockwise orientation.

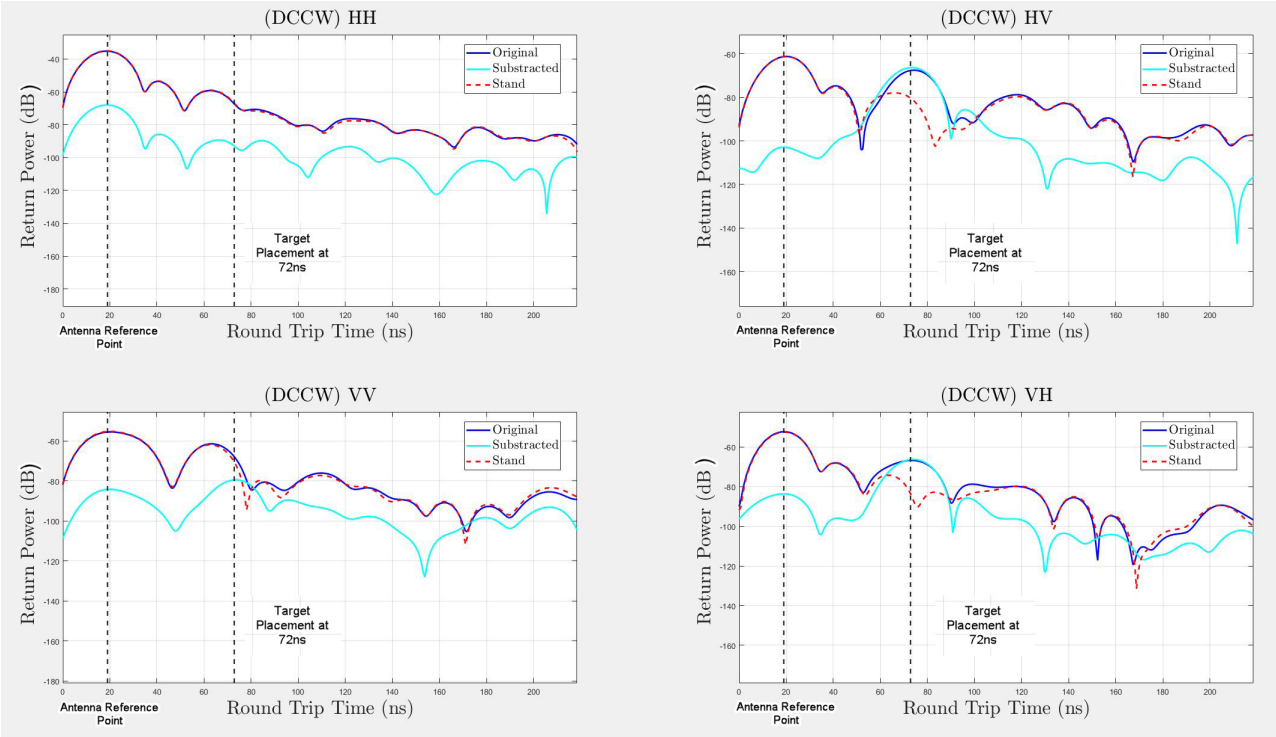

Figure 5.29

Dihedral Counter-Clockwise Response

5.3.2 UAS-Based

The UAS-based scatterometer was assembled in a sealed box for ease of both transportation and mounting on the UAS. The payload is shown in Figure 5.30.

The first test to ensure the RF circuits are operating correctly is to measure their S_{21} response using the Keysight FieldFox in all configurations of the circuit. The first configurations of the circuit will be the cross-polarization measurements. Figure 5.31 illustrates the path of energy flow for the measurement. The expectation of the circuit is the transmit power will increase by 20dB from the RF amplifier and then lose power through insertion losses and coupling losses. All loses illustrated are pulled from the available data sheets on the RF switches and directional couplers.

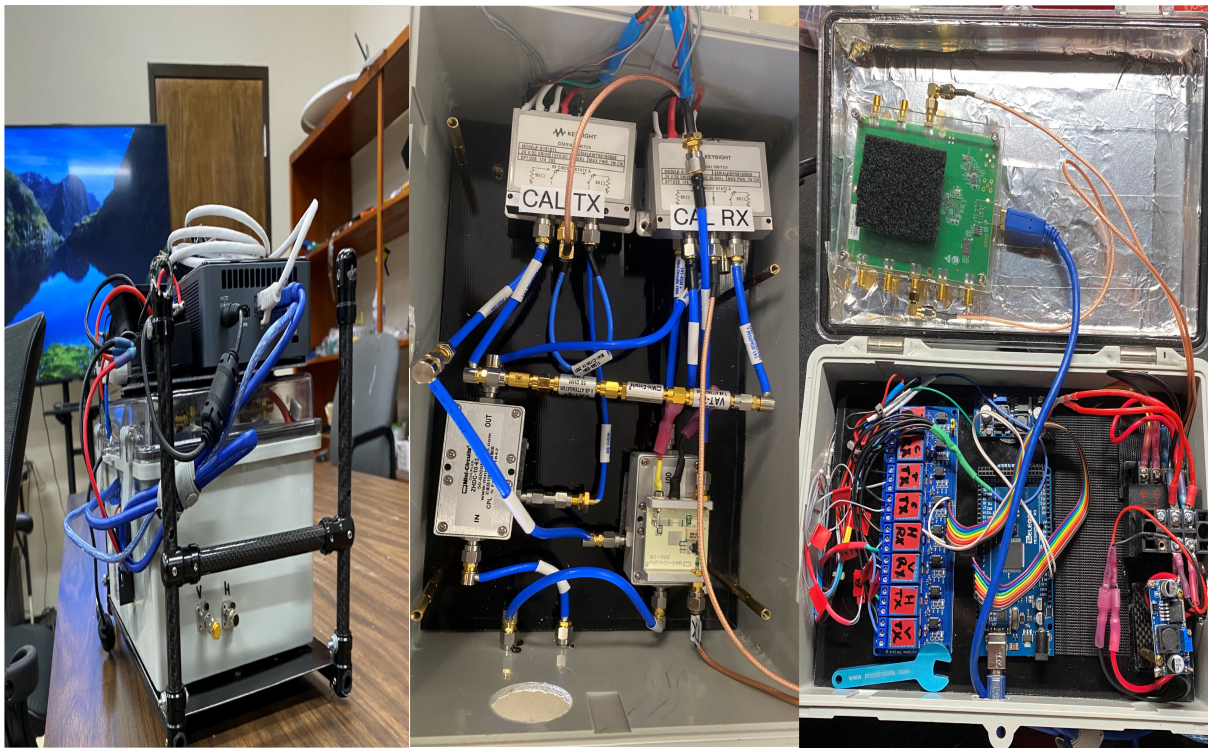

Figure 5.30

UAS scatterometer payload (a) outside view and (b) RF circuit and (c) relay logic circuit

After setting the circuit, the response is shown in Figure 5.32. The responses for both tests show the resulting power is around 4dB higher than the transmit power. There are slight differences in the predicted response and the actual response as well as the differences in the responses of the two circuit of less than 1dB. This can be accounted for in in cable/connector losses. Additionally, the cable lengths and connectors are not identical between the two circuits which validates the slight differences in the responses of the two circuits.

The next test was to verify the isolation between the coupling ports and output ports of the directivity in the co-polarization configurations of the RF circuit. The test circuit is shown in Figure 5.33.

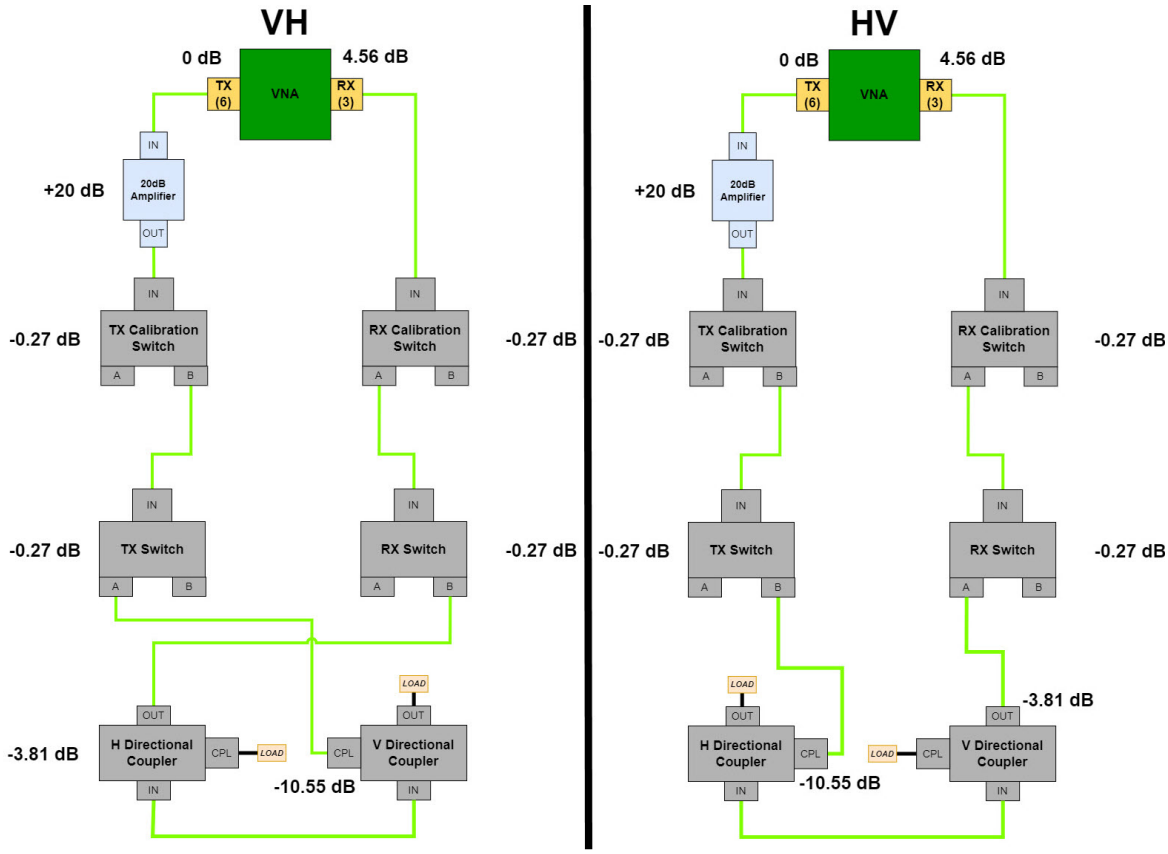

Figure 5.31

Cross-polarization response predictions for UAS (a) VH circuit and (b) HV circuit

After testing the circuit, the response is shown in Figure 5.34. In this test, the signal is again amplified by the 20dB and encounters both insertion losses and coupling losses. The expected loss for the co-polarization responses is -25.24dB and the response from the actual tests has a difference of less than 1dB, again accounted for in the cable/connector losses. This test indirectly validates to the performance of the co-polarization configuration. The directivity states that there is a -36dB difference between the forward power of the output port and the input port from the coupling port. The -26dB S_{21} response validates the directivity and indirectly validates the power transmitted through the input port.

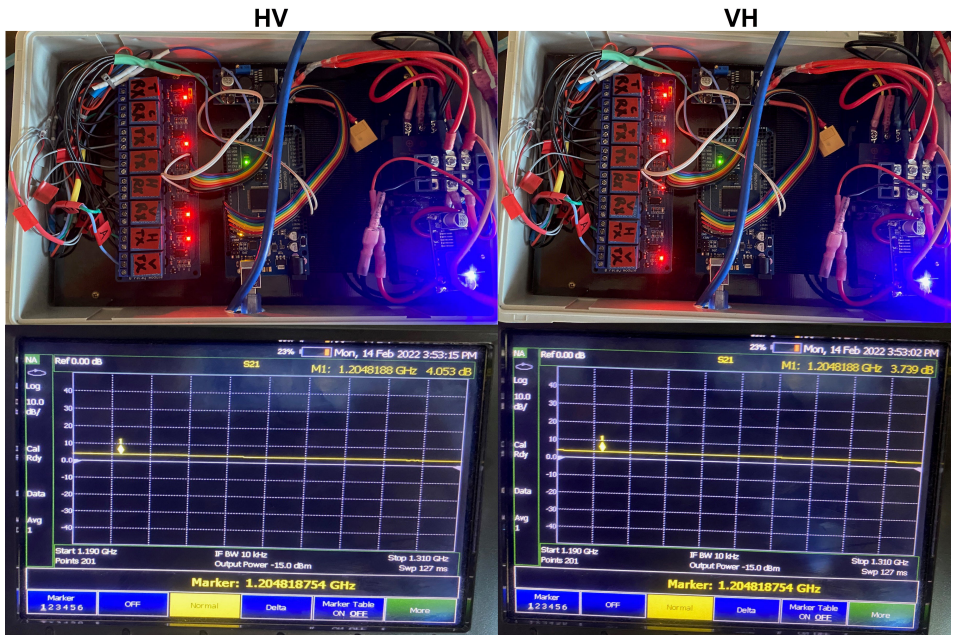

Figure 5.32

Cross-polarization response results for UAS (a) VH circuit and (b) HV circuit

The last test is to verify the response of the calibration circuit. The test circuit is shown in Figure 5.35.

After testing the configuration, the response is shown in Figure 5.36. This response meets expectations as the amplifier is not perfectly stable at 20dB and fluctuates over the band between 20dB-21.5dB over the scatterometer's operating band.

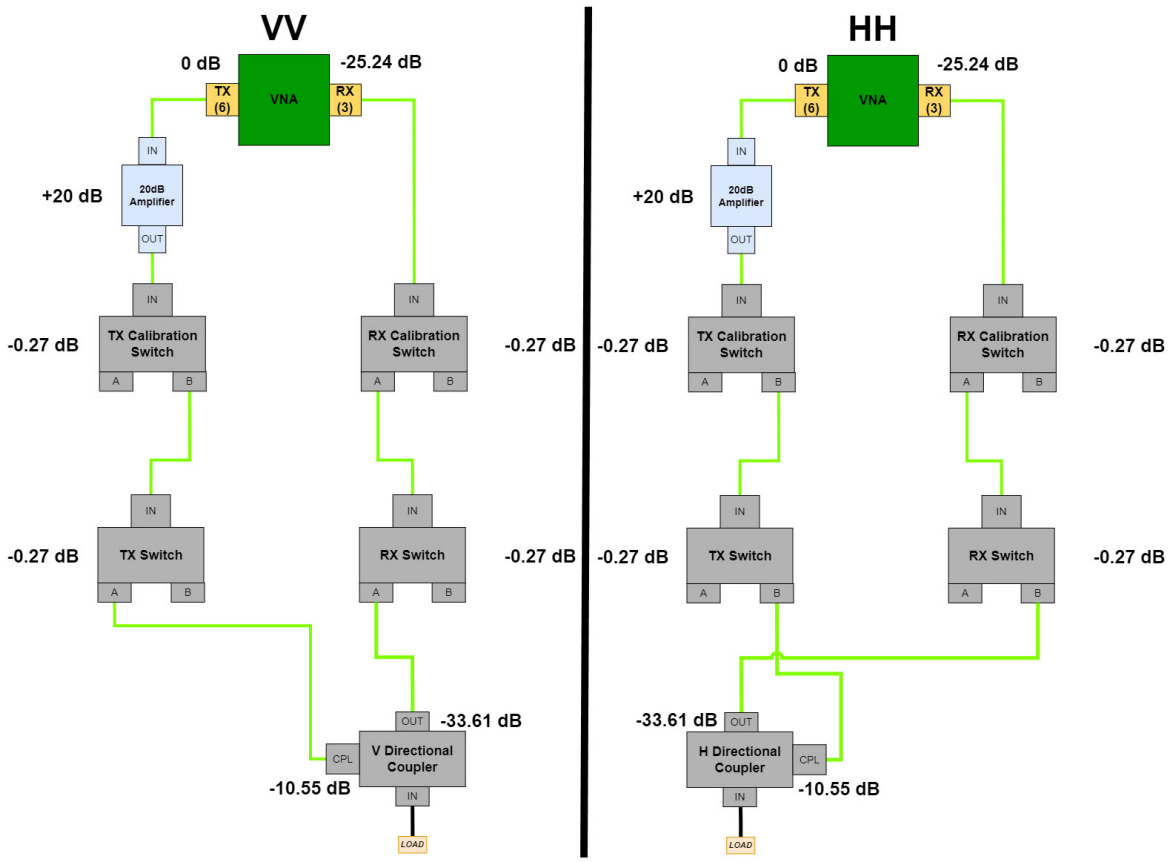

Figure 5.33

Co-polarization response predictions for UAS (a) VV circuit and (b) HH circuit

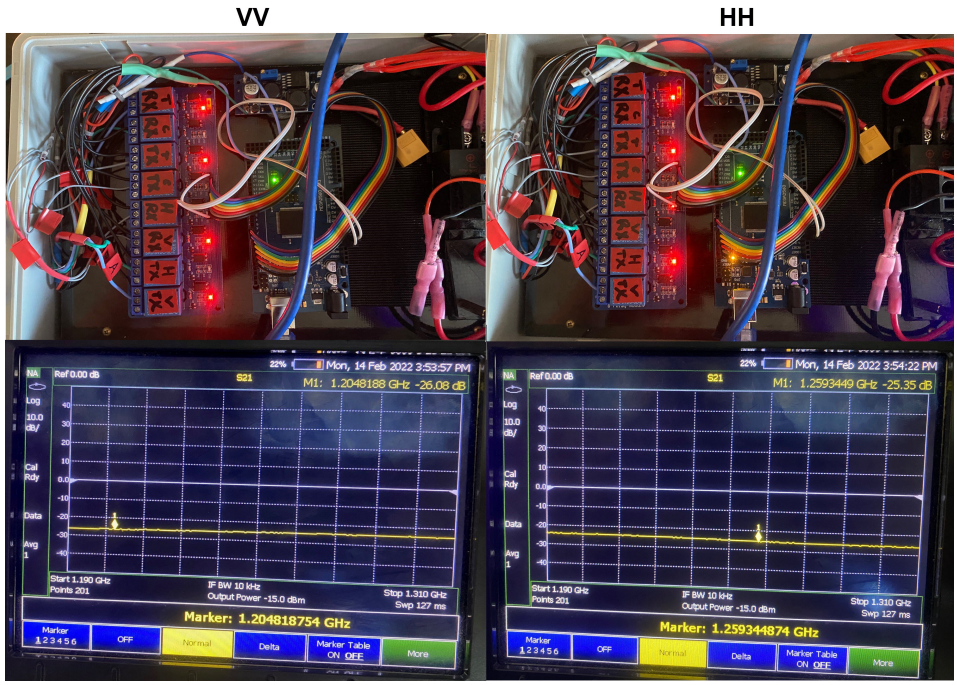

Figure 5.34

Co-polarization response results for UAS (a) VV circuit and (b) HH circuit

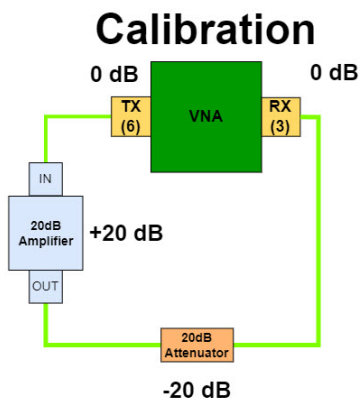

Figure 5.35

Calibration predictions for UAS scatterometer circuit

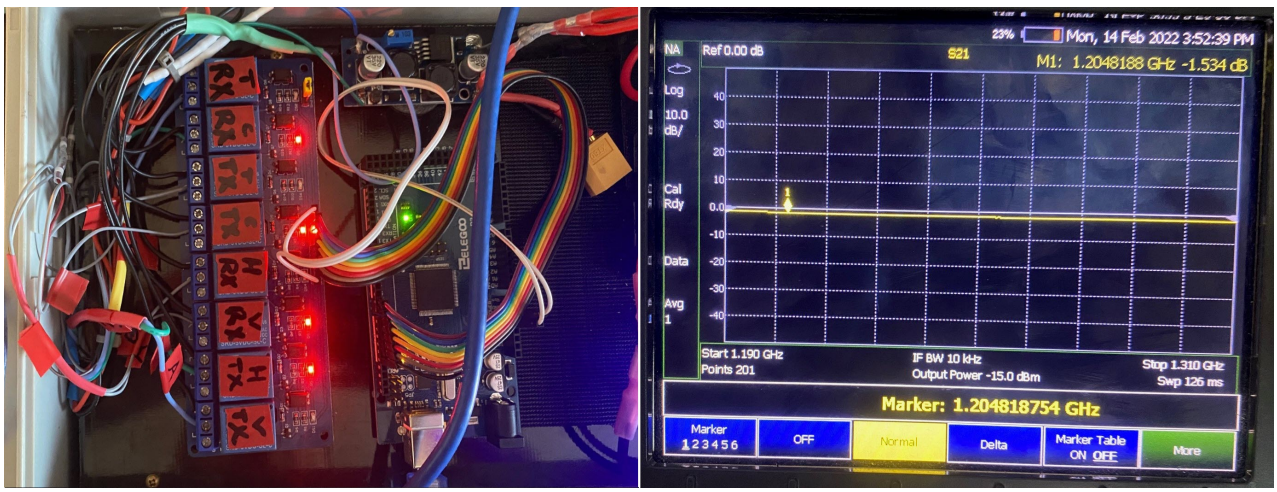

Figure 5.36

Calibration results for UAS scatterometer circuit

CHAPTER VI

CONCLUSION AND FUTURE WORK

This chapter discusses the project results, gives final thoughts, and offers improvements for future work of the created radar systems.

6.1 GPR Improvements

While the GPR system is operable, the system experiences systemic issues due to the flight and control of the UAS. These issues need to be resolved and accounted for in the processing of the GPR data otherwise they will introduce distortions into the data and make the UAS-based GPR data unusable.

Ground Height Normalization

The TF-Mini lidar unit is equipped to the GPR payload and is integrated into the GPR GUI. The testing done in the field with the lidar unit showed that the altitude data collection is possible but needs to be tested further in the field. A post-processing algorithm needs to be developed using the lidar range data to extract the ground reflections from the multiple A-scans autonomously in the already used processing scripts used to create the B-scans.

Ground Surface Localization

The second necessity of the GPR is spatial localization of the UAS. In order to map where the sub-surface are located, the Global Positioning System (GPS) coordinates are needed. These

are already gathered by the UAS for its use in the flight controller. The present issue with using the GPS coordinates from the UAS is that the clock-cycles of its computer system and the GPR computer and separate and not synced to one another. This means the GPS data does not line up in time with GPR data. If the two sets of data can be lined up in time, the fusion of the radar and GPS data becomes trivial.

Traditional GPS works such that the GPS receiver is on the UAS and it communicates directly with global satellites for its position. This is not functional for the UAS as it there is a major trade-off between the time to determine the GPS location and the spatial resolution of the result. While the receiver could return the updated position fast, there would significance spatial variance in the return that would not be useful in mapping the radar data. The GPS unit on the UAS system is a GNSS-RTK receiver that uses a base-station to communicate with satellites to obtain an accurate GPS location. The base-station will spend nearly 30 min to ensure a precise GPS location within 1 meter. With an accurate GPS location, the base-station RTK technology connects with the RTK receiver on the UAS to map the 3-dimensional spatial location of the UAS within spatial accuracy on the order of centimeters.

With accurate GPS data, the next step is to line up the GPS data and the radar data. The GNSS RTK unit, additional to the GPS information, also collects altitude data of the UAS. This altitude data is relative to the base-station, which does not make it fit for replacing the lidar unit as the altitude data would be shifted in space compared to the lidar's altitude data. However, although the data is shifted in time, the relative shape and structure of the altitude data looks similar between the two vectors.

With this basis, the solution to this problem is the development of a calibration procedure to happen before and after every flight. The calibration procedure is shown Figure 6.1. By running this calibration procedure before and after experiments, the altitude data from the lidar unit can be compared to the RTK altitude data and the vectors can be linearly scaled to match each other. The linear scaling factor used to reshape the altitude vectors can then be used to scale the time vector that governs both the GPR and GPS data, solving the radar localization problem.

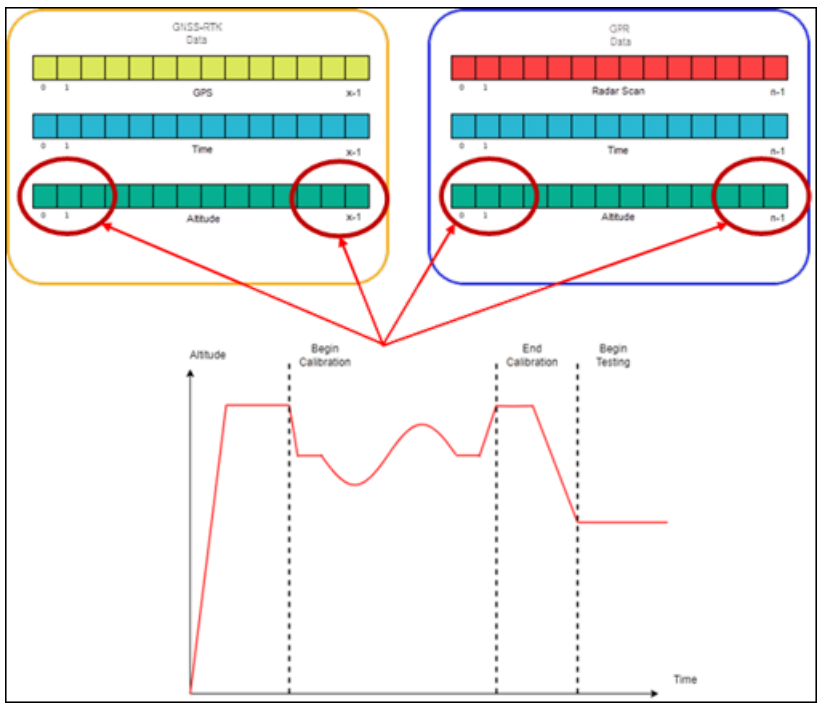

Figure 6.1

LIDAR calibration procedure

6.2 Scatterometer Improvements

The scatterometer circuit for both the ground-based setup and the UAS-setup needs to be tested further in the field to best characterize its performance. Testing of the ground based scatterometer, up until this point, has only been implemented on point/discrete targets. The scatterometer however is meant to image distributed targets and as such needs to be tested further in the field to image distributed targets such as crops, brush, trees, and water.

6.2.1 Calibration

This section describes the mathematical intuition and techniques for calibration of a polarimetric radar with Section 6.3.1 for overview, Section 6.3.2 for first order approximations, and 6.3.3 for cross-polarization calibration of distributed targets.

After data is collected from distributed targets, there is a need to implement an external calibration procedure to interpret the scatterometer data. Unlike point/discrete targets where the echo from the target is meant to be a relatively strong response localized in time, the response from the distributed targets is small as it is a result of backscatter. Additionally, the analysis of the backscatter response to determine characteristics such as soil moisture and surface roughness is predicated on small changes in the data caused by changes in the environment. These changes can be over looked by the radar if the intrinsic noise from the radar is not accounted for in the processing.

6.2.1.1 Overview

As the ground based system is functional for field testing, there is a need to ensure the scatterometer system is returning meaningful data. As a polarimetric radar system, the scatterometer

is concerned with measuring the backscatter in the form of scattering matrices. The scattering matrices are prone to distortions that deviate from the true and expected data [26]. These distortions are caused by factors such as improper frequency response and hardware mismatch, the main contributor of distortion in this system. The use of different cables, antennas, and other RF components skew the data returns and need to be accounted for in the analysis of targets.

The means of calibration for this system will incorporate calibration targets with known backscatter responses, known as external radar calibration. The targets include a metal circular plate and a dihedral reflector. The circular plate will be the main contributor to the calibration correction, but the dihedral reflector is crucial in calibrating the cross-polarization channels.

The following theory explains the mathematical intuition for calibration procedures to correct signal distortions [23] [26]. Given an incident electric field $\hat{E}^i$ composed of both vertical and horizontal components and propagating in the $\hat{k}_i$ direction, the equation is given as:

$$E^i = (E^i_v \hat{v}_i + E^i_h \hat{h}_i) e^{-ik\hat{k}_i r} \tag{6.1}$$

Propagating in the $\hat{k}_s$ direction, the idealized scattered energy with isotropic radiation is given as:

$$E^s = (E^s_v \hat{v}_s + E^s_h \hat{h}_s) = \frac{e^{-ikr}}{r} S E^i \tag{6.2}$$

and as a matrix is expressed as:

$$\begin{bmatrix} E^s_v \\ E^s_h \end{bmatrix} = \frac{e^{-ikr}}{r} \begin{bmatrix} S_{vv} & S_{vh} \\ S_{hv} & S_{hh} \end{bmatrix} \begin{bmatrix} E^i_v \\ E^i_h \end{bmatrix} \tag{6.3}$$

In real-world testing, there are distortions and errors within the scattering matrix to account for due to non-ideal conditions. The first error to account for is those on the transmission side of

the system. There are inherent signal errors in both amplitude and phase, T_{vv} , as well as direct coupling returns between the cross-polarization stages in the transmitter, T_{hv} . Derived from the radar range equation, the scattered energy S from a point target back to the scatterometer from the incident electric field $\hat{E}^i$ is given as:

$$E_s = (\frac{2\eta_0 P_t G_t}{4\pi})^{\frac{1}{2}} \frac{e^{-i2kr}}{r^2} \begin{bmatrix} S_{vv} & S_{vh} \\ S_{hv} & S_{hh} \end{bmatrix} \begin{bmatrix} T_{vv} \\ T_{hv} \end{bmatrix} \tag{6.4}$$

The second point of distortion and error within the scattering matrix stems from the receiver side of the circuit. The receiver also introduces errors into the signal in its phase and amplitude, R_{vv} and R_{vh} . Additionally the receive chain also introduces coupling errors with the cross-polarization returns, R_{hv} and R_{hh}. This yields the received electric field E^r as:

$$E^r = (\frac{G_r \lambda^2}{4\pi})^{\frac{1}{2}} \begin{bmatrix} R_{vv} & R_{vh} \\ R_{hv} & R_{hh} \end{bmatrix} E^s \tag{6.5}$$

Assuming the additional circumstance that the polarization of the transmitter is set to horizontal polarization instead of vertical, the resulting E^r incorporating the transmitter and receiver errors is given as:

$$E^r = K \frac{e^{-i2kr}}{r^2} \begin{bmatrix} R_{vv} & R_{vh} \\ R_{hv} & R_{hh} \end{bmatrix} \begin{bmatrix} S_{vv} & S_{vh} \\ S_{hv} & S_{hh} \end{bmatrix} \begin{bmatrix} T_{vv} \\ T_{hv} \end{bmatrix}, K = \left[\frac{2\eta_0 P_t G_t G_r \lambda^2}{(4\pi)^2} \right]^{\frac{1}{2}} \tag{6.6}$$

Considering the measured scattering matrix M as the idealized scattering matrix multiplied by the transmit and receive distortions, the resulting measured scattering matrix is:

$$\begin{bmatrix} M_{vv} & M_{vh} \\ M_{hv} & M_{hh} \end{bmatrix} = \begin{bmatrix} R_{vv} & R_{vh} \\ R_{hv} & R_{hh} \end{bmatrix} \begin{bmatrix} S_{vv} & S_{vh} \\ S_{hv} & S_{hh} \end{bmatrix} \begin{bmatrix} T_{vv} \\ T_{hv} \end{bmatrix} \tag{6.7}$$

The matrices can be converted to a vectorized form, $M = CS$, which gives:

$$\begin{bmatrix} M_{vv} \\ M_{vh} \\ M_{hv} \\ M_{hh} \end{bmatrix} = C \begin{bmatrix} S_{vv} \\ S_{vh} \\ S_{hv} \\ S_{hh} \end{bmatrix}, C = \begin{bmatrix} R_{vv}T_{vv} & R_{vh}T_{hv} & R_{vv}T_{hv} & R_{vh}T_{vv} \\ R_{hv}T_{vh} & R_{hh}T_{hh} & R_{hv}T_{hh} & R_{hh}T_{vh} \\ R_{vv}T_{vh} & R_{vh}T_{hh} & R_{vv}T_{hh} & R_{vh}T_{vh} \\ R_{hv}T_{vv} & R_{hh}T_{hv} & R_{hv}T_{hv} & R_{hh}T_{vv} \end{bmatrix} \tag{6.8}$$

The density of this expansion can be reduced given a few assumptions. First, there is reciprocity among the cross-pol terms, making them equal. Secondly, the cross-pol coupling is usually 20dB lower than the other terms in a first order approximation, setting $R_{hv}T_{vh}$, $R_{vh}T_{vh}$, $R_{vh}T_{hv}$, and $R_{hv}T_{hv}$ to approximately 0. This reduces C from a 4x4 matrix to a 3x3 matrix. These assumptions and approximations give the new M as:

$$\begin{bmatrix} M_{vv} \\ M_{hh} \\ M_{hv} \end{bmatrix} = \begin{bmatrix} S_{vv} \\ S_{hh} \\ S_{hv} \end{bmatrix} \begin{bmatrix} R_{vv}T_{vv} & 0 & R_{vh}T_{vv} + R_{vv}T_{vh} \\ 0 & R_{hh}T_{hh} & R_{hv}T_{hh} + R_{hh}T_{hv} \\ R_{hv}T_{vv} & R_{hh}T_{hv} & R_{hh}T_{vv} \end{bmatrix}, C = \begin{bmatrix} c_{11} & c_{12} & c_{13} \\ c_{21} & c_{22} & c_{23} \\ c_{31} & c_{32} & c_{33} \end{bmatrix} \tag{6.9}$$

6.2.1.2 First Order Approximation

In this first order approximation, the cross terms in C can be ignored, resulting in a reduced distortion matrix:

$$C = \begin{bmatrix} c_{11} & 0 & 0 \\ 0 & c_{22} & 0 \\ 0 & 0 & c_{33} \end{bmatrix} \tag{6.10}$$

Such that:

$$M_{vv} = c_{11}S_{vv}, M_{hh} = c_{22}S_{hh}, M_{hv} = c_{33}S_{hv} \tag{6.11}$$

Circular Plate

Given the co-polarization returns for the circular plate are equal to one another, they are labeled as S_0 . This reduces the $c11$ and $c22$ as simply:

$$c11 = \frac{M_{vv}^{cp}}{S_0}, c22 = \frac{M_{hh}^{cp}}{S_0} \tag{6.12}$$

Dihedral Vertical

The scattering returns from vertical dihedral may be written terms of the $c11$ and $c22$ values found in the circular plate.

$$S_{vv}^{dv} = \frac{M_{vv}^{dv}}{c11} \rightarrow S_{vv}^{dv} = \frac{M_{vv}^{dv}}{M_{vv}^{cp}} S_{vv}^{cp} \rightarrow S_{vv}^{dv} = \frac{M_{vv}^{dv}}{M_{vv}^{cp}} S_0 \tag{6.13}$$

$$S_{hh}^{dv} = \frac{M_{hh}^{dv}}{c11} \rightarrow S_{hh}^{dv} = \frac{M_{h}^{dv}}{M_{hh}^{cp}} S_{hh}^{cp} \rightarrow S_{hh}^{dv} = \frac{M_{hh}^{dv}}{M_{hh}^{cp}} S_0 \tag{6.14}$$

Dihedral Tilted

The $c33$ can found using the following relations:

$$c33 = \frac{M_{dv}^{dx}}{S_{hv}^{dx}}, S_{hv}^{dx} = \frac{S_{hh}^{dv} - S_{vv}^{dv}}{2} \tag{6.15}$$

Compiling the preceding equations from the circular plate and vertical dihedral tests, the, $c33$ becomes:

$$c33 = \frac{M_{hv}^{dx}}{S_0} \frac{1}{\frac{1}{2}(\frac{M_{hh}^{dv}}{M_{hh}^{cp}} - \frac{M_{vv}^{dv}}{M_{vv}^{cp}})} \tag{6.16}$$

6.2.1.3 Cross Pol Calibration for Distributed Targets

The preceding calibration theory was built around the basis of a point target where the traditional radar cross section (RCS) to be:

$$\sigma_{mn} = 4\pi |S_{mn}|^2 \tag{6.17}$$

The target for the scatterometer, however, is a distributed target and as such, the scattering matrix is inversely proportional to the area of the target of interest. The differential scattering matrix, S^0 is found to be:

$$S_0 = \frac{S}{\sqrt{A}} \tag{6.18}$$

This adapts the cross-polarization incident electric field, E^i_{hv} , to include the rooted area as:

$$E_{hv} = (\frac{r_c}{r})^2 e^{-i2k(r-r_c)} \frac{K}{r_c^2} e^{-i2kr_c} M^{dx}_{hv} (\frac{1}{\frac{1}{2}(\frac{E^{dv}_{hh}}{E^{cp}_{hh}} - \frac{E^{dv}_{vv}}{E^{cp}_{v}})S_0}) \frac{1}{\sqrt{A}} S_{hv} \tag{6.19}$$

The scattering matrix for the distributed target becomes:

$$S_{hv} = E_{hv} \frac{1}{E^{dx}_{hv}} \frac{1}{2} (\frac{E^{dv}_{hh}}{E^{cp}_{hh}} - \frac{E^{dv}_{vv}}{E^{cp}_{vv}}) S_0 \sqrt{A} (\frac{r}{r_c})^2 e^{i2k(r-r_c)} \tag{6.20}$$

resulting in an RCS of:

$$\sigma_{hv}(dB) = 10log_{10}(\sigma_{hv}) = 10log_{10}(4\pi \left| E_{hv} \frac{1}{E^{dx}_{hv}} \frac{1}{2} (\frac{E^{dv}_{hh}}{E^{cp}_{hh}} - \frac{E^{dv}_{vv}}{E^{cp}_{vv}}) S_0 \sqrt{A} (\frac{r}{r_c})^2 e^{i2k(r-r_c)} \right|^2) \tag{6.21}$$

$$\sigma_{hv}(dB) = P_{hv}(dB) - P^{dx}_{hv}(dV) + 10log(A) + 40log(\frac{r}{r_c}) + 10log_{10}(4\pi \left| \frac{1}{2} (\frac{E^{dv}_{hh}}{E^{cp}_{hh}} - \frac{E^{dv}_{vv}}{E^{cp}_{vv}}) S_0 \right|^2) \tag{6.22}$$

The first term $P_{hv}(dB)$ in the RCS represents the uncalibrated return power and the following terms are referred to as the "Calibration Factor" which are recorded and used after calibration experiments to calibrate all future data.

Similar procedures may be done to characterize the RCS for the co-polarization. Where the scattering matrix S_{vv} is:

$$S_{vv} = E_{vv} \frac{1}{E^{cp}_{vv}} S_0 \sqrt{A} (\frac{r}{r_c} e^{i2k(r-r_c)} \tag{6.23}$$

Then the RCS of the scattering is given as:

$$\begin{aligned} \sigma_{vv}(dB) &= 10log_{10}(|E_{vv}|^2) - 10log_{10}(|E^{cp}_{vv}|^2) \\ &+10log_{10}(4\pi|S_0|^2) + 10log_{10}(A) + 40log(\frac{r}{r_c}) \end{aligned} \tag{6.24}$$

$$\sigma_{vv}(dB) = P_{vv}(dB) - P_{vv}^{cp}(dB) + 10log_{10}(4\pi|S_0|^2) + 10log_{10}(A) + 40log(\frac{r}{r_c}) \quad (6.25)$$

Similarly for to σ_{vv} :

$$\sigma_{hh}(dB) = 10log_{10}(|E_h|^2) - 10log_{10}(|E_{hh}^{cp}|^2) + 10log_{10}(4\pi|S_0|^2) + 10log_{10}(A) + 40log(\frac{r}{r_c}) \quad (6.26)$$

$$\sigma_{hh}(dB) = P_{hh}(dB) - P_{hh}^{cp}(dB) + 10log_{10}(4\pi|S_0|^2) + 10log_{10}(A) + 40log(\frac{r}{r_c}) \quad (6.27)$$

where $P_{vv}(dB)$ and $P_{hh}(dB)$ are the uncalibrated responses and the subsequent terms in the equation are those used to calibrate the system.

With these bias values for the measured scattering matrices, the collected responses from the distributed targets can be adequately processed with the radar's intrinsic noise removed.

6.2.2 Improvements to Efficiency

The current configurations for both scatterometer setups utilize a windows PC. These computers while small relative to traditional desktops and laptops, are still heavy and can be replaced with Raspberry Pi 4 computers running Linux. There is support for the UVNA-63 in Linux. This would allow the payload to be made lighter and the UAS flight controller can then be used to enable the scatterometer to begin scanning utilizing the GPIO pins of the Raspberry Pi. This will enable integration with the UAS time clock with the clock of the scatterometer for resolving the GPS location of the scatterometer with the collected radar data. The next thing to resolve are the antennas. The ground-based system utilizes the horn antennas and the UAS-based system utilizes the Vivaldi antennas. These are not the most ideal antennas for this application and they need to be replaced by the patch antennas currently in fabrication.

The UVNA-63 can also be explored further to understand how to utilizes multiple receive ports. An alternative solution to creating a polarimetric radar in lieu of using directional couplers

involves a simple microwave circuit involving one coaxial switch and two RF circulators in addition to the UVNA-63 and the antennas, shown in Figure 6.2. This allows the radar to transmit out of one antenna and then to receive energy into both antennas so that each transmission will yield one col-polarization measurement and one cross-polarization measurement. This will mitigate the coupling losses in the circuit and yield a higher transmit power for the radar. This circuit is predicated on the idea that the UVNA-63 can transmit out of one port and receive into multiple ports. This is possible but idea has not been validated for its efficacy and must be done prior to altering the current RF circuit.

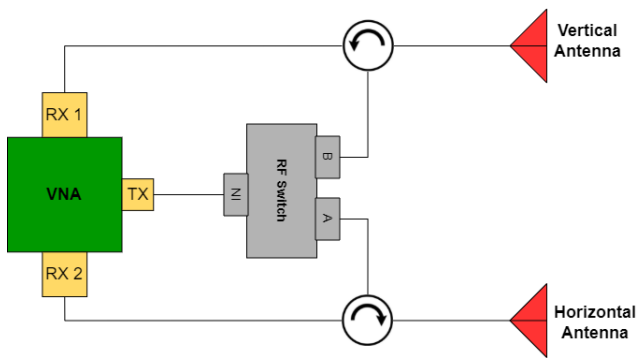

Figure 6.2

RF circuit for polarimetric scatterometer with multiple receive ports

Alternatively, the scatterometer can be implemented with a one-port VNA. In this implementation, the four-polarization circuit can utilize only circulators in lieu of directional couplers. This is beneficial as there will no longer be a substantial loss of power from coupling loss. The circuit can be seen in Figure 6.3 where circulators are used instead of the directional couplers.

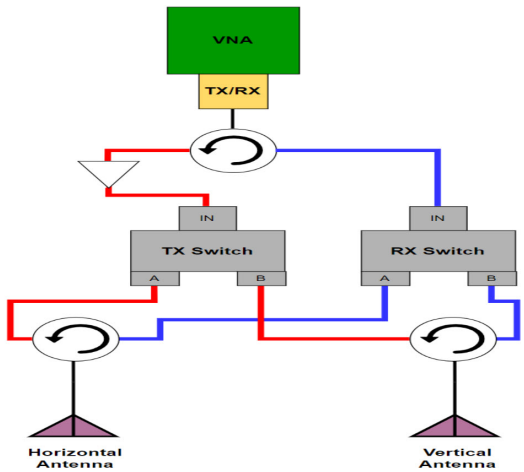

Figure 6.3

RF circuit for polarimetric scatterometer with a one-port VNA using circulators instead of directional couplers

6.3 Final Thoughts

UAS-based radar is a viable means of characterizing the environment. With furthering efforts geared toward refining the fidelity of the technology and mitigating the intrinsic that UAS can introduce, UAS-based radar trends to be one of the predominant means of remote sensing for environmental research in the future. The research discussed in this document lends its self to aiding future work in the development of new UAS-based radar systems that are light weight, robust in operation, and easily accessible to researchers everywhere.

REFERENCES

[1] "The Directional Coupler,", https://www.ittc.ku.edu/ jstiles/723/handouts/The% 20Directional%20Coupler.pdf, Accessed: 2/3/2022.

[2] "Everything RF,", https://www.everythingrf.com/community/what-is-p1db, Accessed: 14/12/2021.

[3] "Ground Penetrating Radar B-scan,", https://www.radartutorial.eu/02 .basics/Ground%20penetrating%20radar.de.html, Accessed: 24/1/2022.

[4] "Measured Quantities,", http://www.av.it.pt/Medidas/data/Manuais%20amp; %20Tutoriais/40b%20-%20VNA%20-%20ZVB20/CD/documents/Help_Files /WebHelp_ZVT/System_Overview/Measurement_Parameters/SParameters.htm, Accessed: 3/1/2022.

[5] "Mini-Circuits UVNA-63,", https://www.minicircuits.com/WebStore/uvna_63.html, Accessed: 10/10/2021.

[6] "Mini Circuits ZX60-H242 Amplifier,", https://www.minicircuits.com/WebStore /dashboard.html?model=ZX60-H242%2B, Accessed: 26/10/2021.

[7] "Pasternack PE15A3008,", https://www.pasternack.com/18-ghz-medium-power-broadband-amplifier-27-db-gain-3.5-db-sma-pe15a3008-p.aspx, Accessed:10/12/2021.

[8] "Radar Equation for Distributed Targets,", https://apollo.nvu.vsc.edu/classes/remote /lecture_notes/radar/conventional/re_distributed.html, Accessed: 25/2/2022.

[9] "RFLambda RAMP00G18GA,", https://www.rflambda.com/pdf /acamplifier/RAMP00G18GA.pdf, Accessed: 15/10/2021.

[10] "RFSPACE Antenna Products,", http://rfspace.com/RFSPACE/Antennas.html, Accessed: 20/12/2021.

[11] "Step Frequency Ground Penetrating Radar Characterization and Federal Evaluation Tests,", https://www.fhwa.dot.gov/publications/research/operations/10037/back.cfm, Accessed:18/1/2022.

[12] "TF-Mini Lidar,", https://www.sparkfun.com/products/retired/14588, Accessed: 12/14/2021.

[13] S. Badjou, D. Kutrubes, and W. Montlouis, "Low-Cost, Lightweight UWB Antenna Design for Humanitarian Drone-Launched GPR Surveys," *2020 IEEE Green Technologies Conference(GreenTech)*, 2020, pp. 181–183.

[14] S. Carey, "Software Defined Radio for stepped-frequency, ground-penetrating radar (Master's thesis)," M.S. thesis, Dept. Electrical and Computer Eng., Georgia Tech. Univ., Georgia, USA., 2017.

[15] M. García Fernández, Y. Álvarez López, A. Arboleya Arboleya, B. González Valdés, Y. Rodríguez Vaqueiro, F. Las-Heras Andrés, and A. Pino García, "Synthetic Aperture Radar Imaging System for Landmine Detection Using a Ground Penetrating Radar on Board a Unmanned Aerial Vehicle," *IEEE Access*, vol. 6, 2018, pp. 45100–45112.

[16] B. Goswami and M. Kalita, "X-band backscattering analysis of soil moisture using ground-based scatterometer," *2015 IEEE Applied Electromagnetics Conference (AEMC)*, 2015, pp. 1–2.

[17] M. Jia, L. Tong, and Y. Chen, "Multifrequency and multitemporal ground-based scatterometers measurements on rice fields," *2012 IEEE International Geoscience and Remote Sensing Symposium*, 2012, pp. 642–645.

[18] S. Kaundinya, E. Arnold, F. Rodriguez-Morales, and A. Patil, "A UAS-based ultra-wideband radar system for soil moisture measurements," *2018 IEEE Radar Conference (RadarConf18)*, 2018, pp. 0721–0726.

[19] M. Kurum, A. C. Gurbuz, S. Barnes, D. R. Boyd, M. Duck, M. M. Farhad, A. Flynt, N. Goyette, P. Peranich, M. Scheider, et al., "A UAS-based RF testbed for water utilization in agroecosystems," *Autonomous Air and Ground Sensing Systems for Agricultural Optimization and Phenotyping VI*. International Society for Optics and Photonics, 2021, vol. 11747, p. 117470J.

[20] S.-G. Kwon, J.-H. Hwang, and Y. Oh, "Soil moisture inversion from X-band SAR and scatterometer data of vegetation fields," *2011 IEEE International Geoscience and Remote Sensing Symposium*, 2011, pp. 3140–3143.

[21] M. Lort, A. Aguasca, C. López-Martínez, and T. M. Marín, "Initial Evaluation of SAR Capabilities in UAV Multicopter Platforms," *IEEE Journal of Selected Topics in Applied Earth Observations and Remote Sensing*, vol. 11, no. 1, 2018, pp. 127–140.

[22] G. Ludeno, I. Catapano, A. Renga, A. R. Vetrella, G. Fasano, and F. Soldovieri, "Assessment of a micro-UAV system for microwave tomography radar imaging," *Remote Sensing of Environment*, vol. 212, 2018, pp. 90–102.

[23] G. Nesti and M. Hohmann, "An efficient calibration procedure for polarimetric radar systems," *10th Annual International Symposium on Geoscience and Remote Sensing*. IEEE, 1990, pp. 1099–1103.

[24] C. Qiu, Y. Chen, L. Tong, M. Jia, and S. Pang, "The method for soil moisture inversion based on ground-based scattering measurement," *2011 IEEE International Geoscience and Remote Sensing Symposium*, 2011, pp. 3086–3088.

[25] M. A. Richards, *Fundamentals of radar signal processing*, McGraw-Hill Education, 2014.

[26] K. Sarabandi, F. T. Ulaby, and M. A. Tassoudji, "Calibration of polarimetric radar systems with good polarization isolation," *IEEE Transactions on Geoscience and Remote Sensing*, vol. 28, no. 1, 1990, pp. 70–75.

[27] C. D. Simpson, S. Kolpuke, A. K. Awasthi, T. Luong, S. Memari, S. Yan, R. Taylor, J. Larson, and P. Clement, "Development of A UAS-Based Ultra-Wideband Radar for Fine-Resolution Soil Moisture Measurements," *2021 IEEE Radar Conference (RadarConf21)*, 2021, pp. 1–4.

[28] D. Sipos, P. Planinsic, and D. Gleich, "On drone ground penetrating radar for landmine detection," *2017 First International Conference on Landmine: Detection, Clearance and Legislations (LDCL)*, 2017, pp. 1–4.

[29] D. Uduwawala, "Gaussian vs differentiated gaussian as the input pulse for ground penetrating radar applications," *2007 International Conference on Industrial and Information Systems*, 2007, pp. 199–202.

[30] F. T. Ulaby, D. G. Long, W. J. Blackwell, C. Elachi, A. K. Fung, C. Ruf, K. Sarabandi, H. A. Zebker, and J. Van Zyl, *Microwave radar and radiometric remote sensing*, vol. 4, University of Michigan Press Ann Arbor, MI, USA, 2014.

[31] J. Wu, L. Wang, W. Zhang, A. Fung, B. Sun, and S. Zhu, "Study on soil moisture with ground-based scatterometer and IEM model," *IGARSS 2001. Scanning the Present and Resolving the Future. Proceedings. IEEE 2001 International Geoscience and Remote Sensing Symposium (Cat. No.01CH37217)*, 2001, vol. 7, pp. 3271–3273 vol.7.

[32] K. Wu, G. A. Rodriguez, M. Zajc, E. Jacquemin, M. Clément, A. De Coster, and S. Lambot, "A new drone-borne GPR for soil moisture mapping," *Remote Sensing of Environment*, vol. 235, 2019, p. 111456.

[33] J. Yan, J. Guo, Q. Lu, K. Wang, and X. Liu, "X-band mini SAR radar on eight-rotor mini-UAV," *2016 IEEE International Geoscience and Remote Sensing Symposium (IGARSS)*, 2016, pp. 6702–6705.